Received: 15 November 2017 | Revised: 8 April 2018 | Accepted: 9 April 2018

DOI: 10.1002/hbm.24186

RESEARCH ARTICLE

WILEY

Effects of *SYN1*$_{Q555X}$ mutation on cortical gray matter microstructure

Jean-François Cabana[1,2] | Guillaume Gilbert[1,2,4] | Laurent Létourneau-Guillon[1,3] | Dima Safi[5,6] | Isabelle Rouleau[3,7] | Patrick Cossette[1,2,3] | Dang Khoa Nguyen[1,2,3]

[1]Centre Hospitalier de l'Université de Montréal (CHUM), Montréal, Québec

[2]Université de Montréal

[3]Centre de Recherche du CHUM (CRCHUM), Montréal, Québec

[4]Philips Healthcare Canada, Markham, Québec

[5]Université du Québec à Trois-Rivières (UQTR), Trois-Rivières, Québec

[6]Groupe de recherche CogNAC (UQTR), Trois-Rivières, Québec

[7]Université du Québec à Montréal (UQAM), Montréal, Québec

Correspondence
Jean-François Cabana, Centre Hospitalier de l'Université de Montréal, 1051, rue Sanguinet, Montréal (Québec) H2X 0C1.
Email: jean-francois.cabana@umontreal.ca

Funding information
Réseau en Bio-Imagerie du Quebec, Grant/Award Number: 13.19

Abstract

A new *Q555X* mutation on the *SYN1* gene was recently found in several members of a family segregating dyslexia, epilepsy, and autism spectrum disorder. To describe the effects of this mutation on cortical gray matter microstructure, we performed a surface-based group study using novel diffusion and quantitative multiparametric imaging on 13 *SYN1*$_{Q555X}$ mutation carriers and 13 age- and sex-matched controls. Specifically, diffusion kurtosis imaging (DKI) and neurite orientation and dispersion and density imaging (NODDI) were used to analyze multi-shell diffusion data and obtain parametric maps sensitive to tissue structure, while quantitative metrics sensitive to tissue composition (T1, T2* and relative proton density [PD]) were obtained from a multi-echo variable flip angle FLASH acquisition. Results showed significant microstructural alterations in several regions usually involved in oral and written language as well as dyslexia. The most significant changes in these regions were lowered mean diffusivity and increased fractional anisotropy. This study is, to our knowledge, the first to successfully use diffusion imaging and multiparametric mapping to detect cortical anomalies in a group of subjects with a well-defined genotype linked to language impairments, epilepsy and autism spectrum disorder (ASD).

KEYWORDS
adult, autism, cortex, dyslexia, epilepsy, genetics, MRI

1 | INTRODUCTION

Many neurodevelopmental conditions, such as autism spectrum disorder (ASD), schizophrenia, epilepsy, and attention-deficit/hyperactivity disorder (ADHD), are believed to have a strong genetic origin (Fischl, 2004; Geschwind, 2011; Hu, Chahrour, & Walsh, 2014; Lewis & Levitt, 2002; Rossignol, 2011; Walsh et al., 2008). Furthermore, some of these conditions, such as ASD, dyslexia, dyspraxia, and epilepsy, are often observed in association (Pagnamenta et al., 2010a; Richardson & Ross, 2000; Schachter, Galaburda, & Ransil, 1993; Tuchman, Moshé, & Rapin, 2009; Tuchman & Rapin, 2002). The increased co-occurrence of these neurodevelopmental disorders suggests that they may share common risk genes. Indeed, we recently reported a *Q555X* mutation on the *SYN1* gene, found in several members of a large French-Canadian family (Fassio et al., 2011). Carriers of both genders are affected by language impairments of different degrees of severity (dyslexia, specific language impairment, speech dyspraxia), while men are furthermore afflicted with focal epilepsy, with two male subjects also suffering from ASD (Nguyen et al., 2015).

SYN1 is a gene on chromosome X involved in encoding synaptic proteins called synapsins, a family of neuron-specific phosphoproteins implicated in vesicular release and transport, synaptogenesis, and synaptic maintenance. *In vitro* studies have shown that this gene plays an important developmental role in neurite outgrowth, and an ongoing role in the distribution of neurotransmitter vesicles and synaptic excitability (Fassio et al., 2011; Fornasiero, Bonanomi, Benfenati, & Valtorta, 2010; Garcia et al., 2004; Lignani et al., 2013).

Although the role of *SYN1* on the development of neurons has been investigated *in vitro*, not much is known about its biophysical repercussion on the adult human brain. In particular, there is no study, to our knowledge, that has investigated *in vivo* cortical gray matter microstructure in a group of subjects affected with *SYN1* dysfunction. Thus, although no apparent macroscopic cerebral anomalies were identified on previous structural MRI of *SYN1*$_{Q555X}$ subjects, we

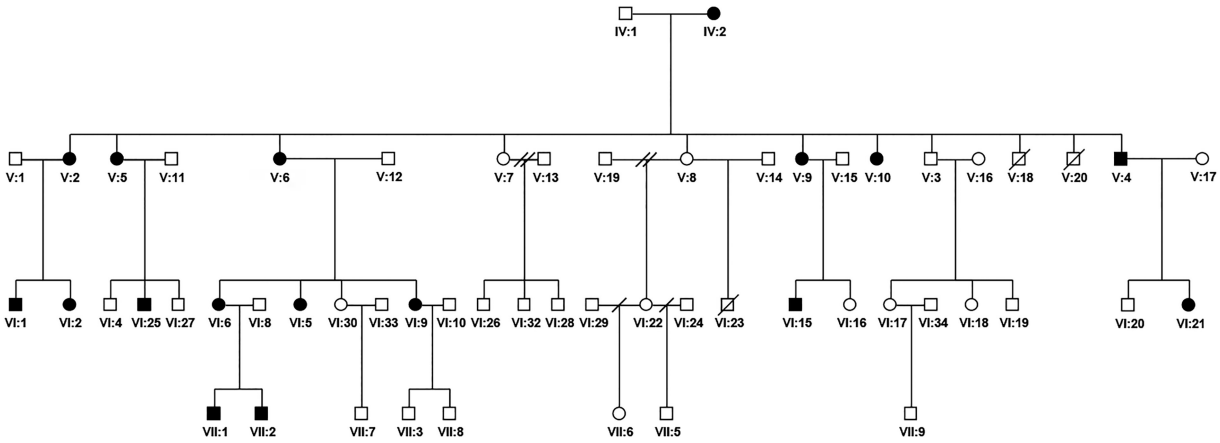

FIGURE 1 Family pedigree. Circles: female subjects, squares: male subjects. Filled symbols show $SYN1_{Q555x}$ carriers

hypothesized that state-of-the-art quantitative MRI modalities sensitive to tissue microstructure and composition could help identify the presence of subtle gray matter alterations. Therefore, we acquired multimodal MRI data from 26 participants: 13 $SYN1_{Q555X}$ subjects (9 female, 18–67 years old; 4 male, 17–52 years old) and 13 age- and sex-matched controls.

Two different MRI modalities were chosen for their complementarity. First, an advanced multi-shell diffusion sequence was acquired. Although diffusion MRI (dMRI) has to date been mostly used to study white matter, recent studies have shown it is also sensitive to cortical microstructure properties, such as radial and tangential fiber populations, and neuropil volume fraction (Jespersen, Leigland, Cornea, & Kroenke, 2012; Kleinnijenhuis et al., 2013; Leuze et al., 2014; Seehaus et al., 2015; Shepherd, Özarslan, Yachnis, King, & Blackband, 2007). Diffusion data was used to estimate diffusion kurtosis imaging (DKI) metrics, including mean kurtosis (MK), fractional anisotropy (FA) and mean diffusivity (MD; Jensen & Helpern, 2010). The NODDI model was also used to estimate the following metrics: intra-cellular volume fraction (ICVF), isotropic volume fraction (ISOVF), and orientation dispersion index (OD; Zhang, Schneider, Wheeler-Kingshott, & Alexander, 2012).

Second, a multi-contrast sequence was used to compute quantitative longitudinal and apparent transverse relaxation times (T1 and T2*), as well as normalized proton density (PD; Jutras, Wachowicz, Gilbert, & De Zanche, 2017). While these metrics are also sensitive to the underlying tissue architecture, they are thought to be mostly sensitive towards tissue *composition*, as opposed to dMRI metrics which are more sensitive to tissue *structure*. For example, T1 and T2* are known to be sensitive to myelin and iron content, while PD and T1 are also non-specific markers of water concentration (Stüber et al. 2014; Lutti et al. 2014; Cohen-Adad 2014; Gelman et al. 2013).

A surface mapping of all these quantitative MRI metrics allowed their characterization and visualization over the full cortical sheet. Compared to traditional voxel-based approaches, bidimensional surface mapping allows for better inter-subject registration of the cortex, and lessens the partial volume contamination with CSF, white matter, or opposite banks of sulci (Glasser et al., 2016).

2 | METHODS

2.1 | Participants

The research protocol was approved by the Centre Hospitalier de l'Université de Montréal (CHUM) Research Ethics Committee, and all subjects gave written informed consent. All 17 members of an extended family carrying the $SYN1_{Q555x}$ mutation identified in a previous study (Nguyen et al., 2015) were recruited (see Figure 1). Of these, four subjects had to be excluded from the current study. The eldest female subject (IV:2) could not participate due to precarious health. Another female subject (V:10) was excluded as she previously suffered a ruptured cerebral aneurysm. A male subject carrying a pacemaker (VI:15) could not pass an MRI examination. Finally, another male subject (VII:1) with more severe ASD was unable to remain motionless during the MRI examination and could not complete the protocol adequately. Hence, 13 $SYN1_{Q555x}$ mutation carriers were included (9 females, 18–67 years old, mean = 45 years old; 4 males, 17–52 years old, mean = 36 years old).

2.1.1 | Clinical observations

In a previous study, all $SYN1_{Q555x}$ mutation carrier subjects were administered an exhaustive neuropsychological test battery including tests sensitive to reading and writing abilities. All $SYN1_{Q555x}$ mutation carriers presented with normal or near-normal intellectual functioning (IQ). Lowest IQ, without verbal-performance dissociation, was observed in male subjects affected with both reflex bathing seizures and moderate to severe dyslexia. Female subjects presented with either mild to moderate dyslexia or some reading/writing difficulties (noted with non-words) not sufficient for the diagnosis of a dyslexic disorder, but confirming the involvement of the phonological pathway present in all $SYN1_{Q555x}$ mutation carriers. Table 1 gives a brief overview of the main neuropsychological findings.

2.1.2 | Subjects matching

Thirteen healthy subjects matched for age and sex were recruited for the control group (9 females, 22–67 years old, mean = 45 years old; 4 males, 19–55 years old, mean = 37 years old). Inclusion criteria for the

TABLE 1 Clinical observations of the *SYN1*$_{Q555x}$ mutation carriers

Subject	Age	Sex	Notes
IV-2	X (79)	F	Intellectual deficit. Excluded from our study due to advanced age and precarious health.
V-2	55 (44)	F	Moderate mixed dyslexia with predominant deficit of the phonological pathway. Speech dyspraxia.
V-4	52 (41)	M	Reflex bathing seizures. Severe mixed dyslexia with predominant deficit of the phonological pathway. Speech dyspraxia.
V-5	67 (56)	F	Mild grapheme-phoneme conversion and spelling difficulties (cannot be classified as dyslexic disorder).
V-6	65 (54)	F	Moderate mixed dyslexia with predominant deficit of the phonological pathway. Mild to moderate speech dyspraxia, associated with mild oro-facial apraxia.
V-9	57 (46)	F	Mild phonological dyslexia. Mild speech dyspraxia, associated with mild oro-facial apraxia.
V-10	X (53)	F	Severe dyslexia of mixed type with predominant involvement of the lexical pathway. Mild speech dyspraxia. Excluded from our study because of a ruptured cerebral aneurism.
VI-1	31 (20)	M	Reflex bathing seizures. Severe dyslexia of mixed type with predominant involvement of the lexical pathway. Speech dyspraxia.
VI-2	25 (14)	F	Mild dysfunction of the lexical pathway + slight involvement of the phonological pathway (cannot be classified as dyslexic disorder).
VI-5	34 (22)	F	Mild mixed dyslexia.
VI-6	42 (31)	F	The profile does not show any dyslexia.
VI-9	39 (28)	F	The profile does not show any dyslexia.
VI-15	X (21)	M	Reflex bathing seizures. Severe mixed dyslexia with predominant involvement of the phonological pathway. Excluded from our study due to pacemaker MRI incompatibility.
VI-21	19 (X)	F	Not evaluated at the time of the neuropsychological study because of her young age, but seemed to present a delay in language development at that time.
VI-25	42 (30)	M	Reflex bathing seizures. Speech dyspraxia. The profile does not show any dyslexia.
VII-1	20 (X)	M	Reflex bathing seizures. Severe ASD. Not evaluated at the time of the neuropsychological study because of his young age. Not included in our study because of severe movement artefacts in MRI data.
VII-2	17 (X)	M	Reflex bathing seizures. Mild ASD. Not evaluated at the time of the neuropsychological study because of his young age.

Age is given at the time of the MRI exam for the current study, and at the time of neuropsychological evaluation for the previous study (in parenthesis). X: Not included in study.

control group included the absence of learning difficulties and of neurological, psychiatric, or language disorders. An independent two-tail *t* test revealed that subject and control groups did not differ significantly in age, intracranial cavity size, total brain volume, bilateral cerebrum volume, or overall movement during examination (see Table 2). Volumetric data was obtained from the *volBrain* segmentation (see Section 2.3.1), while movement data is given by the *eddy* command output (see Section 2.3.2) and represents a summary of the mean total movement in each volume relative to the previous volume during the diffusion sequence acquisition, created by computing the displacement of each voxel and then averaging the squares of those displacements across all intracerebral voxels.

TABLE 2 Subjects and control group comparison

	SYN1$_{Q555x}$	Control	*p* Value
N	13 (9)	13 (9)	1.00
Age	42.2 ± 16.8 (17.4–67.8)	42.8 ± 15.4 (19.3–67.5)	.264
Intracranial cavity (cm^3)	1,378 ± 117 (1,219–1,591)	1,369 ± 159 (1,169–1,693)	.948
Brain size (cm^3)	1,224 ± 111 (1,022–1,367)	1,173 ± 148 (988–1,4700)	.278
Right cerebrum (cm^3)	533 ± 53 (440–605)	508 ± 65 (424–644)	.233
Left cerebrum (cm^3)	534 ± 53 (438–607)	507 ± 65 (420–637)	.204
Movement (mm)	1.16 ± 0.08 (1.04–1.32)	116 ± 0.17 (0.73–1.44)	.707

Values are given as "mean ± *SD* (min–max)", except for *N*, which is "Total (number of females)."

2.2 | MRI acquisition

All MRI acquisitions were performed at the CHUM Notre-Dame Hospital on a Philips Achieva X 3T system equipped with a 32-channel head coil and a high-performance gradient system (80 mT/m). The protocol included the sequences necessary for morphological assessment, multi-shell diffusion-weighted imaging, and multi-contrast imaging targeting quantitative tissue properties. Sequences parameters are given below:

- *Sagittal 3D T1*: Gradient-echo sequence with inversion recovery. TR: 8.1 ms, TE: 3.7 ms, TI: 1,000 ms, spatial resolution: 1 mm isotropic, FOV: 240 × 240 × 170 mm, BW: 191.4 Hz/pixel, SENSE acceleration factor: 2.
- *Sagittal 3D T2*: Turbo spin echo sequence with variable angles. TR: 2,500 ms, TE: 242 ms, spatial resolution: 1 mm isotropic, FOV: 240 × 240 × 170 mm, BW: 934.8 Hz/pixel, SENSE acceleration factor: 4 (2 × 2).
- *Sagittal 3D multi-contrast mapping*: Variable flip-angle multi-echo gradient-echo sequence. TR: 31 ms, TE: 2.3, 4.6, 6.9, 9.2, 11.5, 13.8, 16.1, 18.4, 20.7, 23, 25.3, and 27.6 ms, spatial resolution: 1 mm isotropic, FOV: 240 × 240 × 170 mm, BW: 517 Hz/pixel, SENSE acceleration factor: 4 (2 × 2), flip angles: 6° and 34°.
- *Axial diffusion*: Single-shot spin-echo EPI sequence. TR: 9,000 ms, TE: 78 ms, spatial resolution: 2 mm isotropic, FOV: 224 × 224 × 128 mm, BW: 2,744.0 Hz, SENSE acceleration factor: 2.1. Multi-shell acquisition with 8 $b = 300$ mm^2/s directions, 32 $b = 1{,}000$ mm^2/s directions, 60 $b = 2{,}000$ mm^2/s directions and 6 interleaved $b = 0$ mm^2/s acquisitions. A reference image with reversed phase encoding direction is acquired for the correction of EPI distortions.

2.3 | Data processing

2.3.1 | Structural data

Cortical surface generation and registration

Structural data (T1-weighted and T2-weighted images) was processed using the Human Connectome Project (HCP) processing pipelines (Glasser et al., 2013). The processing included registration across modalities, bias field correction, cortical and white matter surface generation, conversion of *FreeSurfer* output to GIFTI and CIFTI files, and surface registration to the *fs_LR* template (Van Essen, Glasser, Dierker, Harwell, & Coalson, 2012). Parametric maps described below were transferred on each subjects' native cortical surface mesh using a ribbon-constrained volume-to-surface mapping, with the ribbon defined from 25% to 75% of cortical thickness to reduce partial volume contamination with CSF and white matter. Parametric surface maps were then resampled to the common *32k_fs_LR* mesh for group processing.

Sub-cortical gray matter segmentation

To avoid registration issues, we opted to compute metrics for the sub-cortical gray matter structures using a segmentation-based approach. A precise segmentation for each subject was obtained on the T1-weighted image using *volBrain* (http://volbrain.upv.es), an online brain volumetry platform (Manjón & Coupé, 2016). The mask files obtained from *volBrain* were examined for each subject to make sure the segmentation was accurate. The segmentation mask was then used to extract median values for each parametric map, while the volume was given directly in the *volBrain* output. Subcortical structures included left and right caudate nuclei, putamen, thalamus, globus pallidus, hippocampus, amygdala and accumbens.

2.3.2 | Diffusion data

Preprocessing

Raw images were first denoised with the MPPCA algorithm (Veraart et al., 2016; Veraart, Fieremans, & Novikov, 2015), which exploits dMRI data redundancy in the PCA domain, as implemented in MRtrix3 (http://www.mrtrix.org/). A Gibbs ringing correction based on local subvoxel shifts was then applied (Kellner, Dhital, Kiselev, & Reisert, 2015), as it was found that dMRI-derived metrics can be very sensitive to this artefact (Perrone et al., 2015; Veraart, Fieremans, Jelescu, Knoll, & Novikov, 2015). The reverse phase-encoded pair of b0 images was used to estimate the susceptibility-induced off-resonance field using FSL *topup* command (Andersson, Skare, & Ashburner, 2003; Smith et al., 2004). This field estimation output was then fed to FSL *eddy* command, for the simultaneous estimation and correction of eddy current-induced distortions and subject movements (Andersson & Sotiropoulos, 2015). The distortion-corrected dataset was then registered to the T1-weighted image, using the method implemented in the HCP diffusion processing pipeline (Glasser et al., 2013). Data was finally slightly smoothed with a 1.25 mm full width at half maximum (FWHM) kernel to reduce the effect of any residual noise or Gibbs ringing artefacts, as it was found to significantly improve the appearance of dMRI-derived metrics, without losing much details due to smoothing. Results of all intermediate steps were examined visually for each subject to assess the quality of the data and processing. Two diffusion models were then used to compute quantitative parametric maps.

Diffusion kurtosis imaging

Diffusion Kurtosis Imaging (DKI) uses a statistical description of the diffusion-weighted signal (Lu, Jensen, Ramani, & Helpern, 2006). It is a natural extension of diffusion tensor imaging (DTI) that accounts for the non-Gaussian nature of diffusion distribution in restricted environments, such as in biological tissues (Jensen & Helpern, 2010). It was shown to be more accurate than DTI, especially at higher *b* values (Veraart et al., 2011), and could be more sensitive to microstructure changes in disease and aging (Bonilha et al., 2015; Falangola et al., 2008; Grinberg et al., 2016; Guglielmetti et al., 2016; Lee et al., 2014; Steven, Zhuo, & Melhem, 2014). In addition to traditional DTI metrics, DKI also provides indices of radial, tangential, and mean kurtosis, unitless values that quantify the deviation of the diffusion distribution from a Gaussian (Veraart, Sijbers, Sunaert, Leemans, & Jeurissen, 2013). DKI metrics were computed using the *Diffusion Kurtosis Imaging* software (https://github.com/NYU-DiffusionMRI/Diffusion-Kurtosis-Imaging), and the following metrics were used in the group comparison: mean kurtosis (MK), fractional anisotropy (FA) and mean diffusivity (MD). We

should note that metrics common to DTI and DKI (e.g., FA and MD) are not quantitatively the same if computed using one model or the other (Lanzafame et al., 2016; Yan et al., 2013).

Neurite orientation and density imaging

Neurite orientation and density imaging (NODDI) is a physiological model that aims at increasing specificity and sensitivity of diffusion-derived metrics (Zhang et al., 2012). It estimates the complex microstructure related to dendrites and axons using a three-compartment physiological model. The estimation of neuronal density or dispersion is of clinical interest since these aspects are related to cerebral function and can be affected in various pathologies and normal aging (Billiet et al., 2015; Caverzasi et al., 2016; Kunz et al., 2014; Mueller, Lim, Hemmy, & Camchong, 2015; Winston, 2015; Winston et al., 2014). NODDI was shown to be useful in disentangling the contribution of neurite (axons/dendrites) orientation dispersion and density that can be confounded in FA (Zhang et al., 2012). The model was fitted using the Matlab (The MathWorks Inc., Natick) implementation of AMICO (Daducci et al., 2015; https://github.com/daducci/AMICO/), and the following metrics were used in the group comparison: intra-cellular volume fraction (ICVF), isotropic volume fraction (ISOVF), and orientation dispersion index (OD).

2.3.3 | Multi-contrast data

Preprocessing

In order to improve the quality and robustness of the parameters estimation, denoising of the individual echoes was first performed using the AONLM algorithm (Manjón, et al., 2010), as implemented in the *MRI Denoising* software (https://sites.google.com/site/pierrickcoupe/softwares/denoising-for-medical-imaging/mri-denoising). This algorithm was chosen amongst many others as it was found to reduce significantly the noise level while also preserving the details in fine structures. The third echo image of both flip angles series was then extracted and a masked brain image obtained using the FSL BET tool (Smith, 2002). The choice of the third echo was determined as that resulting in optimal brain extraction and registration. Each of the series of images was then individually registered to the T1-weighted reference image. The alignment parameters were determined by using the previously masked brain image and then applied to the complete echo series using cubic b-spline interpolation. The 34° series showed a contrast very similar to the T1-weighted image, and it has been determined that a simple rigid alignment using FSL FLIRT (Jenkinson, Bannister, Brady, & Smith, 2002) resulted in excellent alignment with the reference image. The 6° series showed a different contrast, closer to a PD-weighted image. In this case, the rigid alignment on the T1-weighted image using the FLIRT command proved ineffective. For this reason, we used a boundary-based alignment, as implemented for the registration of diffusion data in the HCP diffusion processing pipeline (Glasser et al., 2013), which was found to work flawlessly in all subjects. Results of all intermediate steps were examined visually to assess the quality of the data processing.

Metric estimation

Preprocessed multi-contrast imaging data was then processed using the VFA-FLASH method presented in Jutras et al. (2017), with slight adaptations. The proposed parameters for the N4ITK B1 bias field correction (Tustison et al., 2010) were found to be suboptimal in our case, and the default options as implemented in the *N4BiasFieldCorrection* command of ANTs v2.1.0 (https://github.com/stnava/ANTs/releases) were used instead. Another difference from the method presented in the method paper (Jutras et al., 2017) is that no smoothing was applied to the T2* map, as denoising of the raw data prior to parameter estimation proved to give better results, without the introduction of additional partial volume effect and loss of details. The following parametric maps were used in the group comparison: longitudinal relaxation time (T1), apparent transverse relaxation time (T2*) and relative proton density (PD). To allow for inter-subject comparison, PD was properly normalized to the mid-point between gray and white matter peaks in the distribution histogram, as described in Jutras et al. (2017).

2.4 | Analyses

2.4.1 | Correlation analyses

Prior to the evaluation of group differences, we performed analyses to assess the relationship between the several metrics used in our study. Individual parametric maps presented above were first averaged across all participants. The group-averaged maps were evaluated visually for qualitative contrast correlations between metrics. Vertex-wise spatial correlation between each metric pair was assessed via a linear regression. The correlation is quantified with respect to the R^2 determination coefficient, and the Pearson r coefficients. Regions affected with susceptibility-induced artefacts (e.g., near frontal sinus or auditory canals) were masked out to avoid biasing the results.

2.4.2 | Group analyses

Individual subjects' parametric maps were first surface-smoothed with a 6 mm FWHM Gaussian kernel. Group-wise differences were then assessed for statistical significance via permutation-based t tests using the PALM software (Winkler, Ridgway, Webster, Smith, & Nichols, 2014). All analyses were conducted with age, sex, age × sex, age^2 and age^2 × sex included as covariates in a general linear model (GLM), using 10,000 permutations, assuming independent and symmetric errors, and corrected for false discovery rate (FDR).

Non-parametric combination

To integrate all metrics into a unified and comprehensive statistical analysis, a two-tail non-parametric combination (NPC) was computed, using the Fisher method (Winkler et al., 2016). NPC is a method to perform joint inference on multivariate data with minimal assumptions. First, each hypothesis is tested separately using synchronous permutations over all parametric maps (i.e., partial tests). The resulting empirical p-values for each partial test are then combined into a joint statistic.

The choice of using the NPC method, as opposed to classical multivariate tests (e.g., MANOVA, MANCOVA, Hotelling's T^2), was made with regards to its simplicity and demonstrated superiority (Winkler et al., 2016). Specifically, NPC was shown to be more powerful, allows an exact control of error rates over the multiplicity of modalities, and needs fewer assumptions than classical multivariate tests. Moreover,

whereas classical multivariate tests such as Hotelling's T^2 generally show a decrease in power as the number of tests is increased, especially when the number of observations (i.e., number of subjects) is low, NPC becomes more powerful as the number of modalities increases, even when the number of variables equals or exceeds the number of observations. As such, given our relatively low number of subjects ($n = 26$) and high number of partial tests ($n = 9$), NPC was deemed the method of choice.

Regions of interest (ROI) analysis

The NPC map was used to identify clusters of highly significant group differences. The clusters were defined as contiguous regions of FDR-corrected p values $< .05$ spanning an area greater than 50 mm^2. ROIs were manually drawn over the identified clusters, to be able to separate groups of clusters that were visually apparently connected. The size and mass of each cluster, defined as the sum of the Fisher statistic of all data points inside a cluster, were computed as quantitative measures of their significance (Bullmore et al., 1999). Median value for each map and each individual subject were obtained in these ROIs, and a one-tail t test was done to characterize group differences in these clusters.

3 | RESULTS AND DISCUSSION

We investigated the cortical microstructure properties of a group of 13 $SYN1_{Q555x}$ mutation carriers, compared to a group of 13 age- and sex-matched controls. The cortex was characterized using two MRI acquisition methods which were deemed *a priori* to complement each other. First, a multi-shell diffusion imaging protocol allowed the evaluation of several metrics sensitive to the structural properties of cortical gray matter. Specifically, DKI was used to compute MK, MD, and FA maps, while NODDI was used to estimate ICVF, ISOVF, and OD. On the other hand, a multi-contrast VFA-FLASH sequence allowed the quantitative estimation of fundamental relaxometry metrics (i.e., T1, T2*, and PD) sensitive to tissue composition, such as water, myelin, or iron content.

3.1 | Inter-parameters spatial correlations

To get a better understanding of the overall properties of the various metrics used in this study, we first explored their spatial correlations and complementarity across the cortex. As both diffusion models (i.e., DKI and NODDI) represent two different ways of interpreting the same data, we expected to find strong correlations between their respective metrics. Inversely, our initial assumption was that dMRI and quantitative relaxometry metrics should complement each other. The metrics were first averaged across the whole cohort to increase signal-to-noise ratio. The maps were then visually examined for qualitative contrast correlations between metrics, and the vertex-wise correlation coefficients between each metric pair were also computed.

Figure 2a shows the group-averaged maps for all metrics. Qualitatively, some broad features are seen to be spatially concordant in several cortical maps. Notably, matching contrasts are seen in the primary motor, premotor and supplementary motor cortices as well as primary somatosensory, visual and auditory cortices, anterior cingulate gyrus and insula. We suggest that this could be explained by the fact that each metric is sensitive to some characteristics of the same underlying environment, with all chosen markers being affected to various degrees by the cyto- and myeloarchitecture. Despite these overall similarities, we also observe that parametric maps derived from the diffusion sequence (top two rows) looks quite different from the metrics from the multiparametric mapping sequence (bottom row). This suggests that combining diffusion data with quantitative multiparametric mapping might prove useful in characterizing the microstructure, by exploiting the sensitivity of these measures to different underlying physical properties of the cortex.

Quantitatively, a strong pairwise correlation (MK-ICVF: $r = .78$, MD-ISOVF: $r = .94$, FA-OD: $r = -.73$) is observed between the two diffusion models (see Figure 2b,c). The strong similarities between MD and ISOVF suggests that any changes found in MD should most likely be also seen in ISOVF, given the very high correlation. This behavior is expected since the isotropic diffusivity compartment represented by ISOVF in the NODDI model is related to the free protons, which exhibit maximum diffusivity. Both relaxation metrics (i.e., T1 and T2*) were also found to be somewhat correlated ($r = .63$). On the other hand, diffusion metrics generally correlated poorly with the multiparametric mapping metrics, suggesting a good complementarity between these two modalities, as assumed *a priori*.

3.2 | NPC analyses

Our study design allowed a characterization of the cortex using a large number of individual parametric maps. However, the identification and interpretation of several spatially concurrent metric changes can be challenging. Moreover, as the statistical power of our study is inherently limited by the size of our unique population, it is possible that subtle microstructural changes could simultaneously affect several metrics in a given location, while still showing up as non-significant on the level of individual parameters. One interesting approach that deals with these issues is to use a non-parametric combination (NPC) statistical model. Indeed, the multiplicity of metrics should be helpful as the power of NPC increases with the number of modalities given as inputs. While the NPC statistic is not informative by itself as to which metric might be affected, its increased power could be useful to identify the location of altered cortical regions. The identification of these regions in turn can be used to interpret our findings in relation to the neuropsychological phenotype of our population.

Figure 3 shows the NPC statistic of a two-tailed t-test, displayed as -log(p), for $p < .05$, which represents the probability of altered microstructure, all metrics combined. Clusters of FDR-corrected p value $\leq .05$ and area ≥ 50 mm^2 were identified as regions where the most significant changes were observed. The relative mass index for these clusters, defined as the sum of all statistics inside a cluster, normalized to the largest cluster mass, was computed as a quantitative measurement of alterations extent, that is a larger mass is indicative of larger microstructural changes, in terms of statistics and size. This index thus represents a way to identify which cortical regions are most affected in our group of $SYN1_{Q555x}$ carriers.

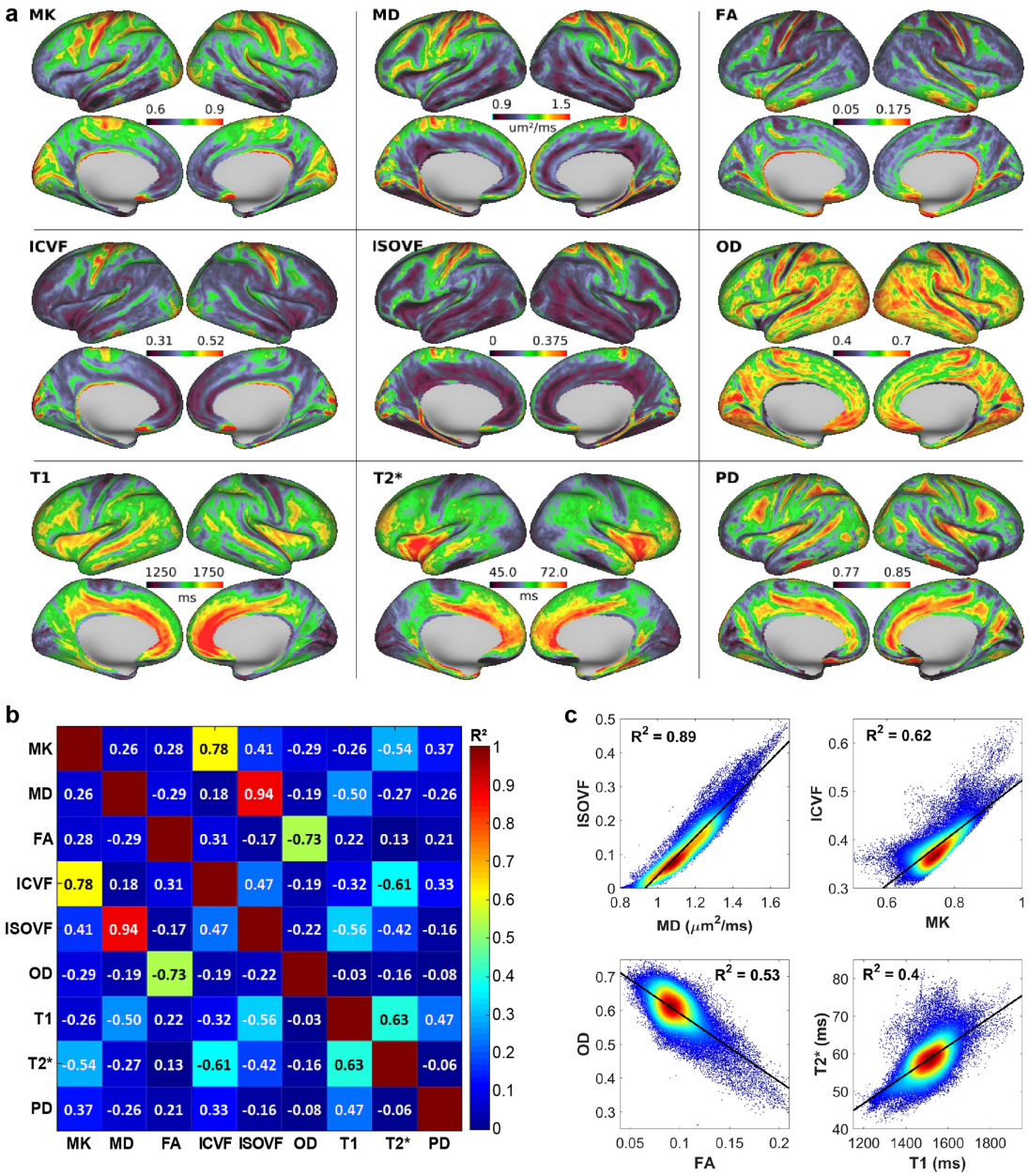

FIGURE 2 Group-averaged parametric maps. (a) Mean parametric maps for all 26 subjects. (b) Across cortex vertex-wise correlation coefficient between each metric pair. The matrix is color-coded with respect to the R^2 determination coefficient, and numbers on the figure are the Pearson r coefficients. (c) Vertex-wise scatter plots of the four most correlated metric pairs, color-coded by density [Color figure can be viewed at wileyonlinelibrary.com]

Twenty-two clusters were found, and their anatomical location, size and relative mass are described in Table 3. The mass index indicates that the most affected regions are located in the right hemisphere, that is the inferior-anterior part of the supramarginal gyrus (cluster #16, normalized mass = 1.0), the occipito-parieto-temporal junction (#13, mass = 0.806), the superior temporal gyrus (#11, mass = 0.468), and posterior collateral sulcus (#22, mass = 0.355). In the left hemisphere, the most significant clusters were located on the anterior part of the superior frontal gyrus (#10, mass = 0.283), the posterior part of the middle temporal gyrus (#2, mass = 0.260) and the insula (#1, mass = 0.185).

3.2.1 | Contribution of individual metrics to NPC

The results obtained above using the NPC multivariate method are obviously dependent on the inputs given to the algorithm, that is the joint distribution depends on the partial tests. Moreover, we have shown how the metrics from DKI and NODDI were highly correlated with each other. To get an idea of how the choice of including the parametric maps presented above influenced the identification of altered cortical regions, we performed additional analyses by successively excluding individual metrics in the NPC step.

First, as both diffusion models seemed redundant, we excluded all three maps from the NODDI model, to see if any information would be

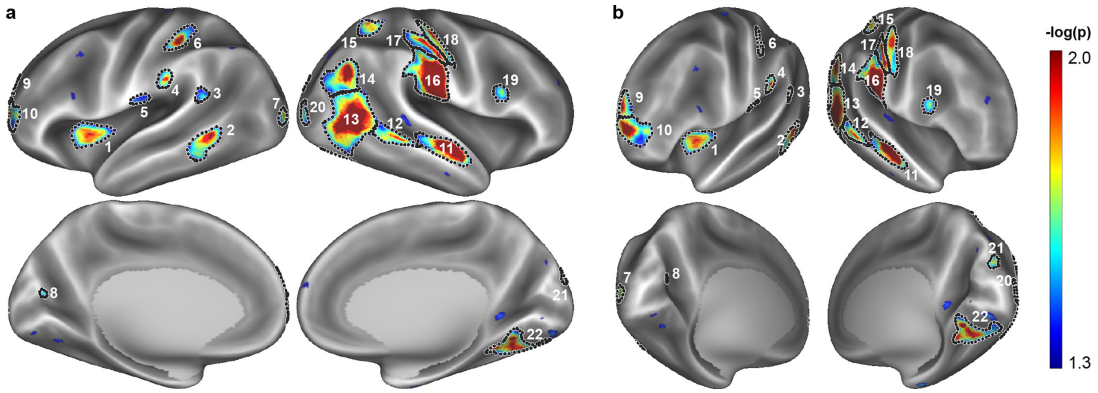

FIGURE 3 Non-parametric combination statistics of all metrics, showing clusters of significant differences between $SYN1_{Q555X}$ and control groups. FDR-corrected p values are shown as $-\log(p)$, from $p = .05$ (blue) to $p = .01$ (red). Clusters of FDR-corrected p value $\leq .05$ and area ≥ 50 mm^2 are identified with a black border and a number used throughout this article. Grayscale background image represents the group-averaged curvature map, that is sulcus in light gray and gyrus in dark gray. (a) Lateral-medial view on inflated, group-averaged surfaces; (b) antero-posterior oblique view [Color figure can be viewed at wileyonlinelibrary.com]

TABLE 3 Identification of significantly altered clusters location, size, and relative mass

# Left hemisphere	Location	Position	Size (mm^2)	Mass
1	Insula	Superior/anterior	272	0.185
2	Middle/inferior temporal gyrus	Posterior	346	0.260
3	Supramarginal gyrus	Inferior/posterior	62	0.058
4	Supramarginal gyrus	Inferior / anterior	94	0.084
5	Postcentral gyrus	Inferior	73	0.061
6	Postcentral gyrus	Posterior	147	0.185
7	Lateral occipital sulcus	Posterior	85	0.059
8	Cuneus/pericalcarine cortex	Anterior	57	0.019
9	Superior frontal gyrus	Anterior	170	0.108
10	Superior frontal gyrus	Anterior	447	0.283
Right hemisphere				
11	Superior temporal gyrus	Inferior/anterior	547	0.468
12	Middle temporal gyrus	Posterior	362	0.204
13	Inferior parietal lobule/Lateral occipital cortex	Anterior	831	0.806
14	Inferior parietal lobule	Posterior	435	0.306
15	Superior parietal lobule	Anterior	163	0.174
16	Supramarginal gyrus	Inferior/anterior	727	1.000
17	Postcentral gyrus	Posterior	286	0.284
18	Postcentral gyrus	Anterior	451	0.328
19	Precentral sulcus	Inferior	49	0.048
20	Lateral occipital sulcus	Posterior	70	0.054
21	Superior parietal lobule	Inferior/posterior	64	0.039
22	Collateral sulcus	Posterior	572	0.355

Clusters were identified on the NPC map as regions of contiguous FDR-corrected p value $< .05$ and area > 50 mm^2. Location was determined from the group-averaged gyrus-based segmentation and curvature maps. Relative mass is defined as the sum of all statistics inside a cluster, normalized to the largest cluster mass

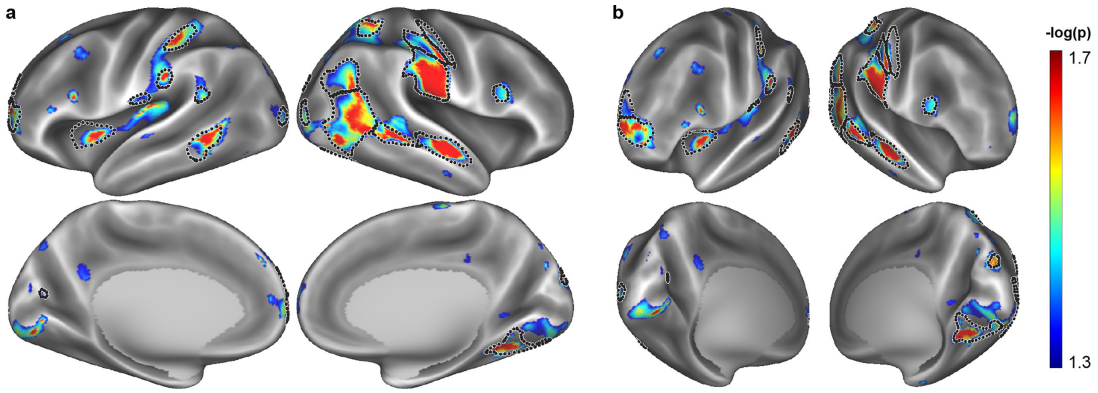

FIGURE 4 FDR-corrected NPC results, excluding the NODDI parametric maps from the analyses, presented on (a) lateral-medial view on inflated, group-averaged surfaces and (b) antero-posterior oblique view. Note that the black borders shown on this figure are the same as Figure 3, that is they represent the clusters of significant cortical alterations, as found by the NPC analysis on all data, including NODDI [Color figure can be viewed at wileyonlinelibrary.com]

lost when only DKI is considered. Results of this analysis are shown in Figure 4. It is apparent that the exclusion of NODDI metrics from the analysis had a very subtle effect. Overall, the distribution of clusters appears mostly unchanged, thus indicating that most of the information given by NODDI is still present in the DKI maps. However, we also see some notable differences such as the apparition of a new cluster in the posterior part of the left insular cortex and the disappearance of cluster #18, on the anterior bank of the right hemisphere postcentral gyrus. These results suggest that while DKI metrics largely reflects the same information as NODDI metrics, both models can complement each other.

Continuing from this NODDI-less NPC map, we successively removed one parametric map at a time from the NPC analysis, and evaluated how each one affects the results. As shown in Figure 5, the exclusion of MK, T1 or T2* from the dataset barely affected the results at all. On the other hand, excluding MD had a dramatic impact, as no FDR-corrected cluster was found. This shows that MD was the main contributor to the observed alterations. Excluding FA or PD also had a large impact on the results, as an overall decrease in -log(p) was seen (increased p values), while several clusters disappeared altogether. These results point to an important contribution of these two metrics to the overall distribution of altered clusters.

3.2.2 | Clusters analysis

To better characterize the observed cortical alterations, we performed a ROI based one-tail t test on the clusters defined in Figure 3. This test allowed a detailed view of the characteristics observed in each of these clusters, and a global view of the patterns observed across clusters. Figure 6 clearly shows that the significant decrease in MD/ISOVF is found consistently across all clusters. An increase in FA is also notable for all

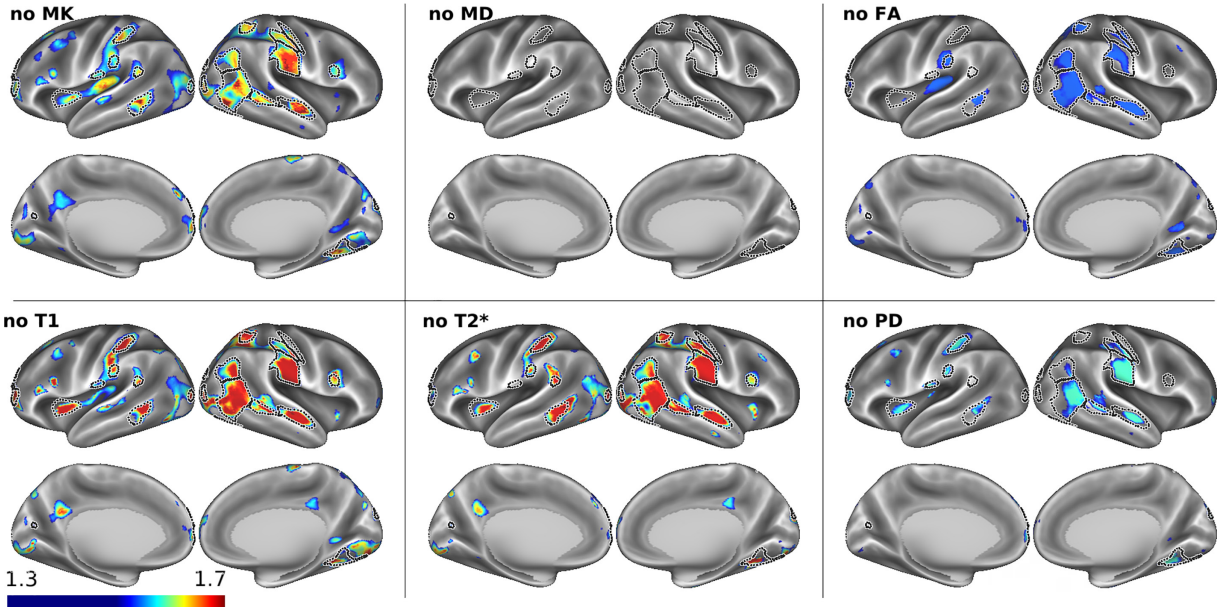

FIGURE 5 FDR-corrected NPC results, excluding the NODDI parametric maps from the analyses, and excluding one more metric at a time. Color scale represents −log(p) [Color figure can be viewed at wileyonlinelibrary.com]

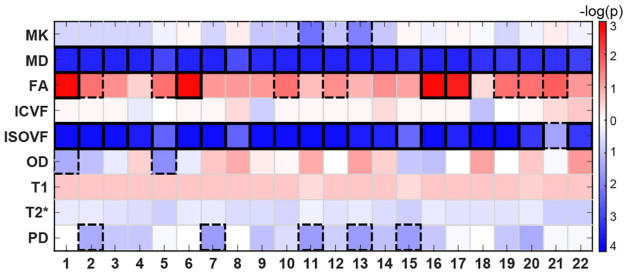

FIGURE 6 Detailed results on the clusters identified above. Numbers on *x*-axis represent clusters number. One-tailed statistics for all metrics, displayed as $-\log(p_{FDR})$. Blue: $SYN1_{Q555X}$ < control; Red: $SYN1_{Q555X}$ > control. Results for $p_{FDR} < .05$ and $p_{FDR} < .005$ are highlighted with dashed and solid lines respectively [Color figure can be viewed at wileyonlinelibrary.com]

regions, but this increase is not significant everywhere. Four clusters (1, 6, 16, and 17) with $p < .005$ were found in FA, and seven others (2, 5, 10, 19, 20, and 21) with $p < .05$. On the opposite, OD, which could be considered the counterpart of FA (see Figure 2), showed a significant decrease in only two clusters (1 and 5), while also showing increased values elsewhere, although not significant. This indicates that while FA and OD generally show opposite trend across the cortex, they can in fact vary differently on a more local level. It could also be indicative of a noisier behavior of OD, leading in a higher variability across subjects, and thus a decrease in sensitivity. Proton density (PD) is also found to be significantly decreased in several clusters (i.e., 2, 7, 11, 13, and 15). Other significant changes include two clusters of decreased MK (11 and 13). Finally, a consistent increase in T1 and decrease in T2* are found across all clusters, although this trend was not significant.

3.2.3 | Single ROI analyses

The next step in our analysis was to take all the clusters defined above as a single region of interest (ROI), in order to evaluate the distribution of the mean values on an individual subject level. This allowed us to assess the robustness of the previous findings, and determine if the observed trends were present in all subjects.

First, the mean value for all parametric maps were obtained for each subject, using all previously defined clusters taken together as a single large ROI. These values were then used to plot the values distribution across subjects, and to perform a new two-tail *t* test. Figure 7 shows the results of this analysis, with the data taken after regression of the GLM. The significant diminution in MD and ISOVF found previously in all clusters is well represented by the difference in group mean values. The distributions are well defined, and the values do not seem largely driven by outlying subjects. The same can be said about the significant augmentation of FA and diminution of PD, although in these cases there is a bit more overlap between the two groups distribution. In this ROI test, we also observe a significant ($p < .05$) diminution in MK in the subject group, although the effect seems small compared to the dataset size and variance. This figure also shows that the higher T1 and lower T2* values in the subject group cannot be regarded as significant, as the group distributions overlap largely.

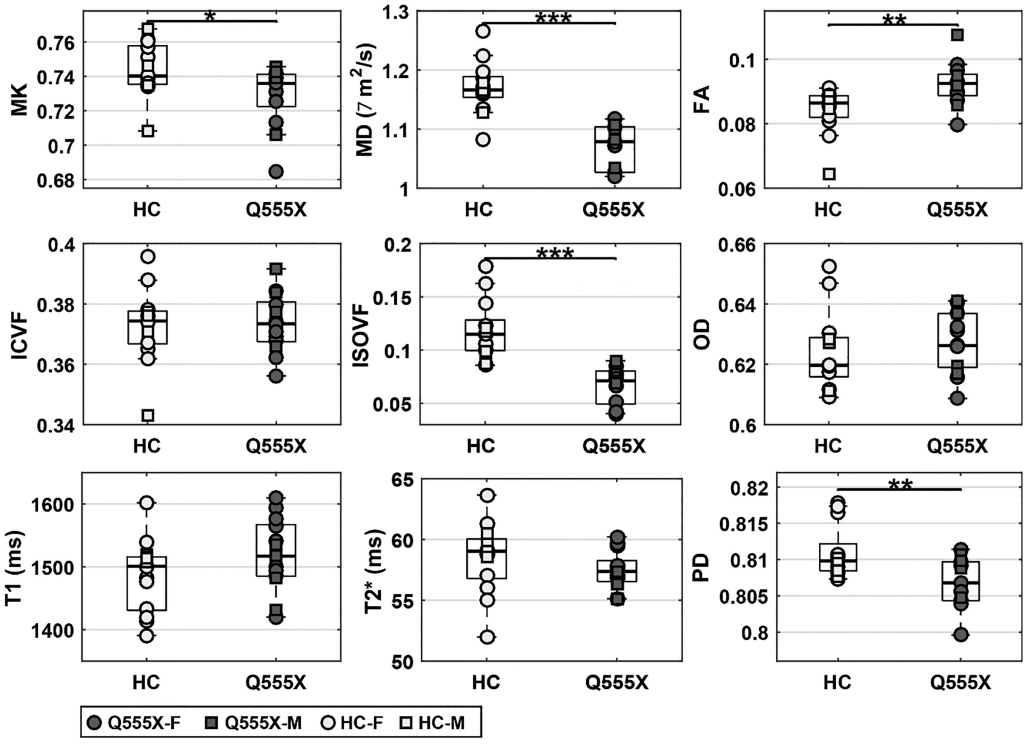

FIGURE 7 Analysis of mean values over all the identified clusters taken as a single ROI. Data points represent mean values for each participant. On each box, the center mark indicates the median value, and the top and bottom edges indicate the 25th and 75th percentiles, respectively, while whiskers extend to extreme values not considered outliers. Stars and lines show significant results of the two-tailed *t* test at $^{*}p < .05$, $^{**}p < .01$, $^{***}p < .001$

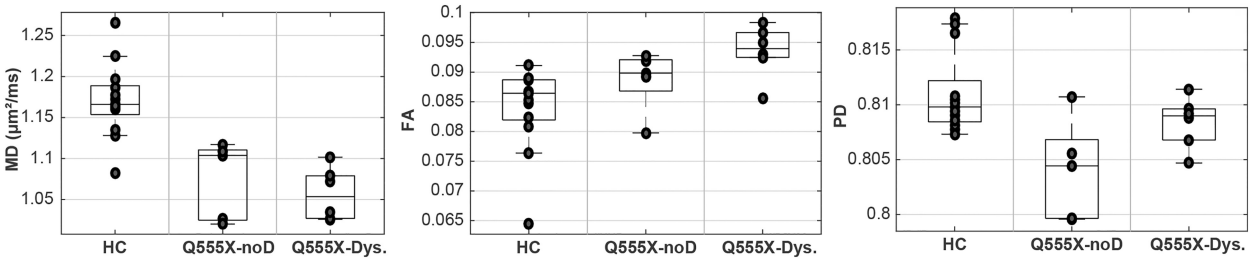

FIGURE 8 Microstructure characteristics of typical readers and dyslexic subjects. Data represents mean values across all identified clusters. HC: healthy control subjects; Q555X-noD: subjects carriers of the $SYN1_{Q555x}$ mutation, but not affected by dyslexia; Q555X-Dys: subjects carriers of the $SYN1_{Q555x}$ mutation and diagnosed with dyslexia

Clinical phenotype sub-groups

Our subjects group was characterized by a wide range of clinical phenotype. Let's recall that in our group of 13 $SYN1_{Q555x}$ carriers, six were diagnosed with varying degrees of dyslexia, four had reflex bathing seizures, and one had mild ASD. To help disentangle the effects of the genetic mutation with that of the clinical phenotypes, we performed additional analyses by dividing the $SYN1_{Q555x}$ group in sub-groups classified by clinical phenotype.

As not all the subjects in the $SYN1_{Q555x}$ group were diagnosed with dyslexia, we first looked at whether there was a difference in microstructural properties between $SYN1_{Q555x}$ subjects with or without dyslexia. Figure 8 shows the distribution of mean values across all identified clusters for the control group (HC), $SYN1_{Q555x}$ subjects without dyslexia (Q555X-noD) and with dyslexia (Q555X-Dys). The significant decrease found previously in MD and PD is observed in both $SYN1_{Q555x}$ sub-groups, regardless of diagnosis. This suggest that these alterations could be a direct consequence of the mutation itself, and not an effect of having dyslexia. The observed increase in FA is also present in both $SYN1_{Q555x}$ sub-groups, but the effect appears stronger in the dyslexic group. These results suggest that FA could be indicative of the language impairments severity in the $SYN1_{Q555x}$ group. We should note nonetheless that the limited sample size limits the interpretability of these results.

Given the observed sex-dependent phenotype, that is male subjects being clinically more affected than females (more severe dyslexia, addition of epilepsy and/or ASD), we hypothesized that we would find more severe alterations in the male than the female group. To verify this hypothesis, we looked at the distribution of mean values across all the clusters taken as a ROI. Figure 9 shows box plots of subject groups separated by gender. Overall, the significant decrease in MD and increase in FA is quite evident, but we did not observe a stronger effect in the male group. Interestingly though, T2* seemed to be more affected in the male group, while the decrease in PD seemed more prominent in the female group. It is however worth mentioning again that segregating our subjects in subgroups lowers the statistical power considerably given the limited number of subjects.

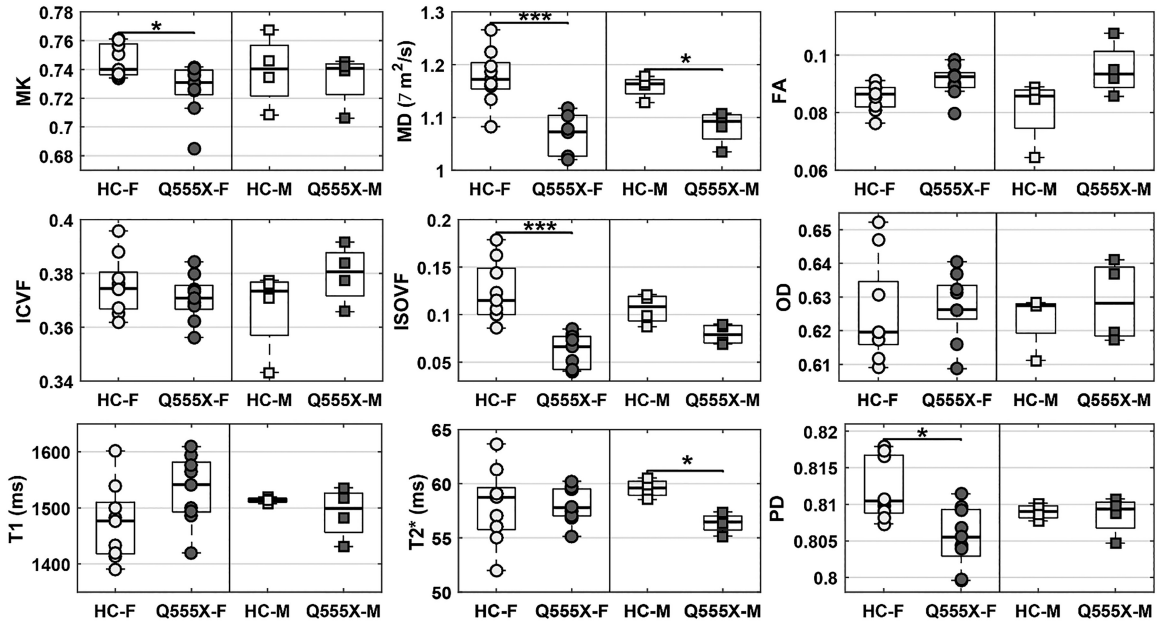

FIGURE 9 Gender-based group differences. Data represents the mean value across all identified clusters for each subject, separated by gender and by group (control vs. $SYN1_{Q555x}$). On each box, the center mark indicates the median value, and the top and bottom edges indicate the 25th and 75th percentiles, respectively. Whiskers extend to extreme values not considered outliers. Lines and stars above box pairs indicate a significant difference was found (*$p < .05$, **$p < .01$, ***$p < .001$) on a two-tail t test

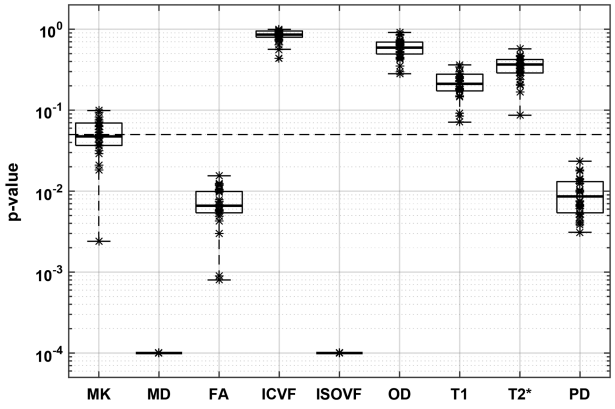

FIGURE 10 Results of the leave-one-out analysis on the ROI data. Stars indicate the p value for each iteration of the test. Dashed line indicates the $p = .05$ level. Note that results for MD and ISOVF were all equal to $p = .0001$, which is the limit achievable in the test performed with 10,000 permutations

3.3 | Additional analyses

3.3.1 | Leave-one-out test

As the sample sizes were relatively low in both the subjects and control group, we performed additional analysis to assess the robustness of our findings, and rule out the possibility of a single or a few outliers that could bias the results. Using the same ROI dataset as above, that is the subject-level mean values across all identified clusters, a two-tail t test was performed repeatedly following the removal of a single subject from the dataset. Figure 10 shows the results of this test, as a distribution of p values for all parametric maps. These results demonstrate clearly that the findings of alterations in MD, ISOVF, FA and PD are all very robust, as all iterations of the test still rendered p value $< .05$. In fact, all results for MD and ISOVF gave a p value $= .0001$, which is the absolute limit achievable in our test design, that is with 10,000 permutations.

3.3.2 | Morphological assessment

The relative thinness of the cortex (~2–5 mm) compared to the MRI resolution (2 mm isotropic in our case for dMRI), implies that cortical parametric mapping is inevitably sensitive to partial volume contamination with adjacent CSF and/or white matter voxels. It is thus important to assess for possible morphological differences between our groups to see if different degrees of partial volume effect could explain the observed microstructural changes. For example, it could be possible that the decrease in MD observed in the $SYN1_{Q555x}$ group was due to a decreased contribution of CSF, which exhibit very high diffusivity. An increase in cortical thickness (less partial volume with CSF) could then be responsible for decreased MD.

Thus, we conducted additional independent one-tail t tests on cortical thickness as well as curvature, as both of these morphological features could have an impact on partial volume effect. Figure 11 shows the results of this test. We observe various regions of higher or lower curvature and thickness throughout the cortex, but none of these changes survived FDR correction. Importantly, we see that these changes do not correlate with the clusters of significant alterations observed previously on the NPC map, as shown with the black borders on Figure 13. Moreover, we observe either apparently randomly distributed increase or decrease in curvature and thickness, which is inconsistent with the overall changes in MD, which was shown to be decreased globally. Consequently, partial volume effect can effectively be disregarded as a possible leading cause of the observed changes.

3.3.3 | Population

One aspect of this work on which we obviously had no direct control was the choice of subjects. Given that the $SYN1_{Q555x}$ mutation was only specifically found in this extended family, we wanted to maximize the number of subjects by including all family members with the mutation who could successfully perform the MRI exam. As such, our subjects group is somewhat heterogeneous with regards to gender (9 female vs. 4 males) and spans a wide age range (17–67). This heterogeneity can be limiting when trying to evaluate possible small changes compared to controls, especially given the relatively small sample size.

We accounted for the group variability in the study design, by matching each subject to a control of the same sex and age group (within 5 years). However, even given the comparability of groups with regards to gender and age, it remains that these variables could account for a large portion of the variance for some metrics. As the null hypothesis in the permutation tests used here was tested by shuffling the residuals sign (i.e., cohort mean subtracted data), it is of paramount importance to remove as much variance as possible to increase

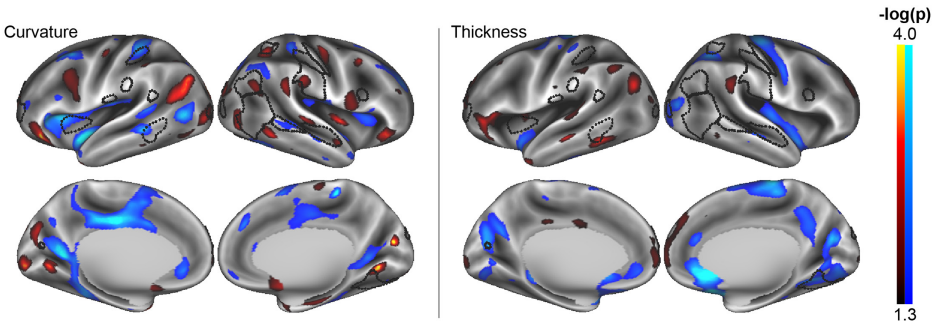

FIGURE 11 Results of the one-tailed t test for structural metrics, shown as $-\log(p_{uncorr})$. Regions in blue represent $SYN1_{Q555X} <$ control, whereas regions in red represent $SYN1_{Q555X} >$ control. The black borders represent clusters of microstructural alterations, as identified previously (see Figure 3) [Color figure can be viewed at wileyonlinelibrary.com]

statistical power. Age and gender was thus included in our GLM, such that the variance associated with these variables was regressed out of the data prior to the residuals sign permutations. To account for the fact that some parameters could have a non-linear relationship with age, we also included age^2 in the covariates. Finally, given the possibility that the age effect could be different with gender, combinations between age and gender were also included in the GLM. Specifically, all analyses were conducted with age, sex, age $\times$ sex, age^2 and age^2 $\times$ sex included as covariates. It should be noted however that there may be a risk of overfitting the age and sex effects given the small number of participants, and that a simpler design without the inclusion of covariates might have been more conservative. Results of an NPC analysis with this simpler design (not shown here) showed that the distribution of altered regions remains essentially the same as in Figure 3, although in this case the findings do not survive FDR correction due to a considerably lower statistical power.

To evaluate the contribution of age to the variance of the parametric maps, a linear and quadratic fit was performed to show how each metric varies with age and age^2. Figure 12a shows the mean values across the whole cortex for all individuals, plotted against age. Linear and quadratic fit R^2 value are given on the figure, which represents the proportion of the variance that is explained by these covariates. A significant relationship with age is seen for most of the metrics. Specifically, MK, ICVF, MD, and ISOVF all show a linear increase with age, with up to 62% of the variance explained by age in the case of MK. T1, T2*, and PD all showed a somewhat linear decrease with age, although age^2 obviously did explain a bit more variance, up to 49% in the case of T2*. Finally, FA and OD both showed an apparent quadratic relationship with age. Given the inverse correlation between these metrics observed across the cortex earlier (see Figure 2), it is not surprising to see how FA and OD show opposite variation with age. Yet, this observation indicates that the relationship between these metrics is present not only spatially across the cortex, but also with age. In this case, OD was the most highly correlated with age^2, with an R^2 of 0.49. An increase in OD (decrease in FA) is observed up to age 40, with the opposite relationship past this age.

Figure 12b shows the same data as in Figure 12a, but after regression of all covariates. This figure clearly demonstrates how our GLM design neatly removes much of the data variance, thus allowing the evaluation of the split between subjects and controls group mean values.

3.3.4 | Subcortical gray matter

Although the main focus of our study was to investigate cortical gray matter properties, our data also allowed the characterization of subcortical gray matter structures. The mean values for all parametric maps in left and right subcortical structures were used to perform an independent two-tail *t* test. Figure 13 shows the results for this test.

Contrary to what is found in the cortex, MD and FA do not seem to be significantly affected, but ICVF, ISOVF, and T1 are altered in some structures. These results show that two structures in the right hemisphere are mostly affected in the $SYN1_{Q555x}$ group, that is caudate nuclei and thalamus. These structures both showed lowered ICVF and ISOVF compared to control. An increase in T1 is also observed, though only significant in the caudate nuclei, while the thalamus showed a significant decrease in MK The fact that alterations are found predominantly in the right hemisphere agrees with what was observed in the cortex, and could be indicative of altered connectivity in the cortico-striato-thalamic network.

3.4 | Interpretation of findings

3.4.1 | Relation between microstructure alterations and clinical phenotypes

The surface-based approach and combinatory analyses used in this study allowed for a much higher sensitivity and specificity than what is usually seen in traditional voxel-based studies. Indeed, it is difficult to get a proper inter-subjects registration of the complex and variable cortical structure using a volume-based approach. Because of this, most cortical studies have been severely affected by a lack of proper inter-subject alignment over the full cortex, which limits sensitivity to detect changes in small, localized regions. Moreover, this study is, to our knowledge, the first to use quantitative metrics sensitive to tissue microstructure and composition over the whole cortex in a population with a well-defined genotype linked to dyslexia, epilepsy and ASD. Nevertheless, we can compare our unique results with previous studies to validate if our findings agree with results from other imaging modalities. As the main condition throughout our subjects group is a language impairment, we first compare our results with reported studies in dyslexia.

Prior research in dyslexia examined cerebral volumetrics, functional activation, structural and functional connectivity in gray and/or white matter structures, but none has yet considered gray matter microstructure (Bailey, Hoeft, Aboud, & Cutting, 2016; Baillieux et al., 2009; Caylak, 2009; Cui, Xia, Su, Shu, & Gong, 2016; Elnakib et al., 2014; Finn et al., 2014; Frye et al., 2011; Lebel et al., 2013; Maisog, Einbinder, Flowers, Turkeltaub, & Eden, 2008; Paulesu, Danelli, & Berlingeri, 2014; Pollack, Luk, & Christodoulou, 2015; Rimrodt, Peterson, Denckla, Kaufmann, & Cutting, 2010; Tamboer, Scholte, & Vorst, 2015). Our results showed an alteration in gray matter microstructure in dyslexic subjects in several regions, with the most affected ones being the supramarginal gyrus (SMG), the occipito-parieto-temporal junction, the superior temporal gyrus (STG) in the right hemisphere as well as the superior frontal gyrus (SFG), the middle temporal gyrus (MTG) and the insula in the left hemisphere. Several altered regions (e.g., bilateral MTG, SMG, and the occipito-temporal junction) are in good agreement with previous findings of neuroimaging studies in reading and dyslexia. Indeed, these regions are generally viewed as part of the "reading-writing" pathway and have been showed to be either under- or over-activated in dyslexics (Barquero, Davis, Cutting, Tolvanen, & Lyytinen, 2014; Maisog et al., 2008; Price, 2012; Richlan, Kronbichler, & Wimmer, 2009, 2011; Rimrodt et al., 2009; Shaywitz & Shaywitz, 2008). On the other hand, a new finding of our study is the alteration observed in the SFG. We suggest that this alteration can be explained by the contribution of the SFG to higher cognitive functions, executive processing and working memory, which are particularly involved in

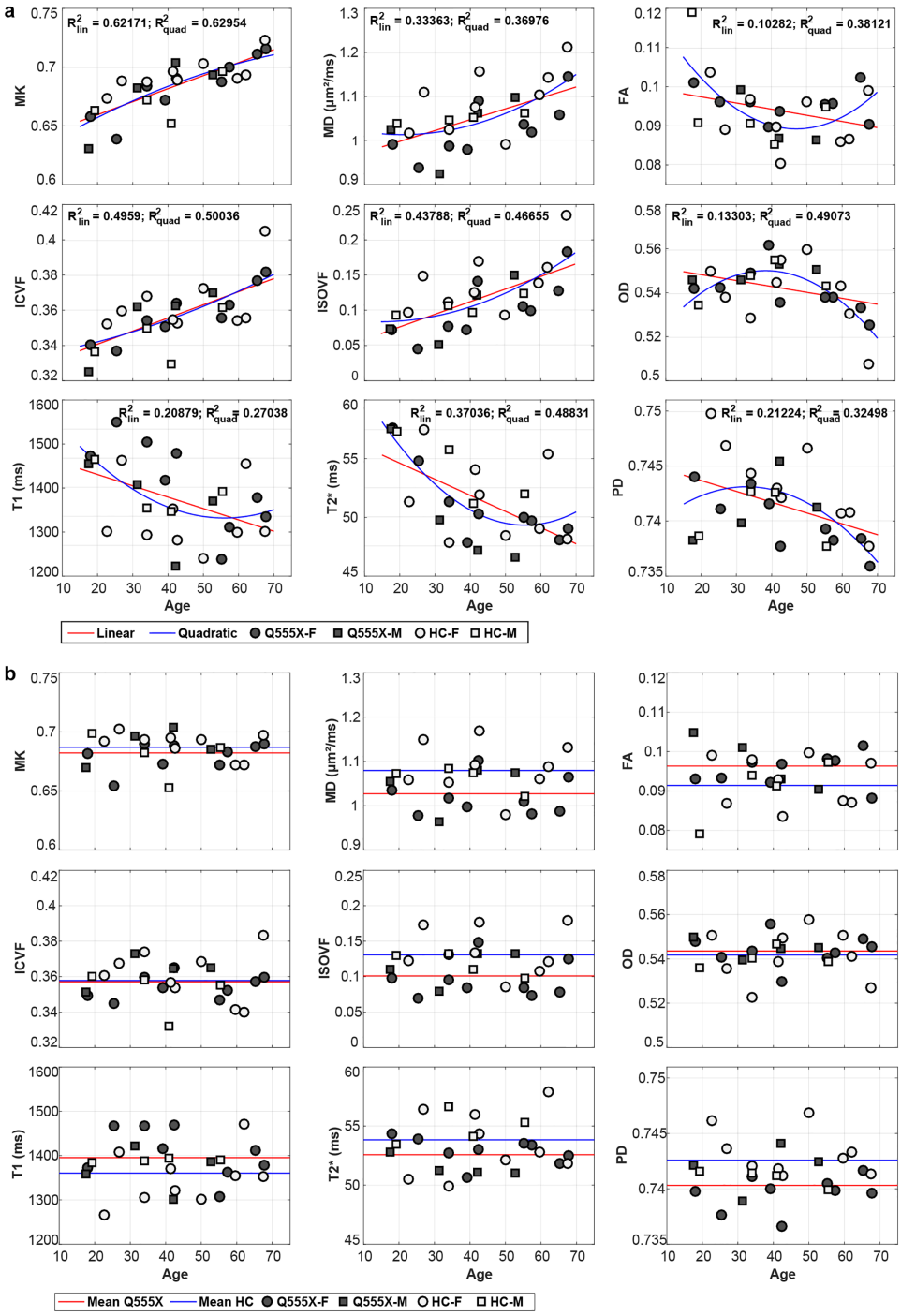

FIGURE 12 Whole cortex parametric maps mean values variation with age. Each data point represents the mean value over the whole cortex for an individual. (a) raw data, prior to regression of covariates. The linear (red) and quadratic (blue) relationship with age is displayed, and its R^2 value given in legend. (b) data after regression of covariates. Red and blue lines here represent the subjects and control group means [Color figure can be viewed at wileyonlinelibrary.com]

reading comprehension (Boisgueheneuc et al., 2006; Cain, 2006; Carretti, Borella, Cornoldi, & De Beni, 2009).

With regards to our clinical observations on the epileptic subjects reported before, the significant group differences found here are concordant with the "parieto-insulo-temporal epileptic network" initially proposed based on seizure semiology, ictal electroencephalographic (EEG) recordings and functional imaging (Nguyen et al., 2015). Indeed, affected males had seizures often featuring early somatosensory symptoms and frequently triggered by the contact of water, suggesting activation of the parietal cortex but also the insula, a key integrative multisensory region. In addition, seizures captured on scalp EEG in a patient showed epileptiform discharges over the right temporal region. Finally, single photon emission computed tomography (SPECT) showed right temporo-insular hyperperfusion during seizures in two patients.

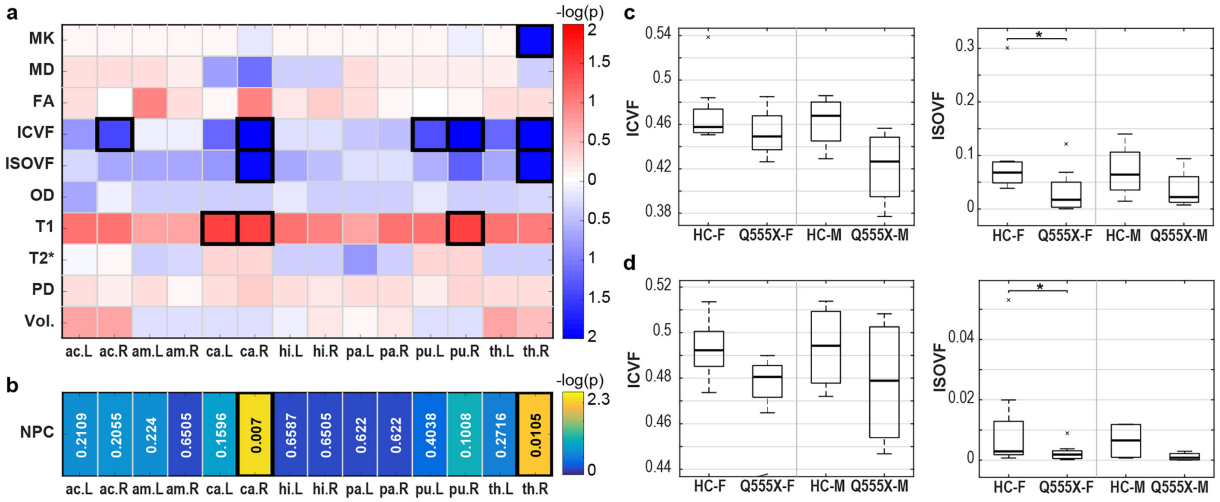

FIGURE 13 Results for the group comparison of subcortical gray matter structures. ac: accumbens, am.: amigdala, ca.: caudate nuclei, hi.: hippocampus, pa.: globus pallidus, th: thalamus, L: left hemisphere, R: right hemisphere. (a) One-tailed statistics for all metrics, displayed as $-\log(p_{FDR})$. Blue: $SYN1_{Q555X}$ < control; Red: $SYN1_{Q555X}$ > control. Results for $p_{FDR} < .05$ are highlighted with solid lines. (b) NPC statistics. Color scale is displayed as $-\log(p_{FDR})$, and numbers on the figure show the actual p_{FDR} value [Color figure can be viewed at wileyonlinelibrary.com]

3.4.2 | Hemispheric asymmetry

Although there is no definitive evidence for a left-right lateralization in epilepsy, ASD or dyslexia in general, it seems to be the case in our well-targeted group of subjects. While these neurodevelopmental conditions might be of various origin, it seems plausible in our case that they could be linked specifically to the $SYN1_{Q555X}$ mutation. One could thus speculate that the observed asymmetry is in part gene-specific (i.e., $SYN1_{Q555X}$-specific), although the downstream mechanistic pathways are largely unknown. In addition, this asymmetry could in part be related to the epileptic condition affecting four of our subjects. Indeed, analysis of multimodal neurophysiological data suggested an epileptic focus in the right hemisphere for 3 of them (unknown for the other; Nguyen et al., 2015). Prior morphological studies in patients with focal epilepsy have revealed subtle atrophy distributed predominantly ipsilateral to the side of seizure onset, maximum within the epileptogenic lobe but also in more distant regions (Bernhardt, 2010). These morphological changes suggest that tissue microstructure might also be predominantly affected in the hemisphere of the epileptic focus.

Moreover, observations of a predominantly affected right hemisphere have been reported by others. Indeed, functional neuroimaging studies have often revealed atypical lateralization and involvement of the right hemisphere in dyslexic subjects when compared to typical readers. Previous reports on dyslexia showed a left–right hemispheric imbalance in either under- or over-activation of reading-writing related cerebral regions, as well as loss or reversal of cerebral asymmetry in certain brain regions, such as planum temporale, perisylvian, or parietooccipital region (Farmer & Klein, 1995; Galaburda et al., 2006a; Valdois et al., 2004; Waldie et al., 2017). These results, combined with the present study, suggests that an altered hemispheric asymmetry, reflecting atypical organization of the right hemisphere, may be a defining feature of dyslexia.

3.4.3 | Cortical microstructure model

Although the exact action mechanism of the *SYN1* gene in the human brain is not yet fully understood, it is known that synapsins play an important role in neuronal development, cytoskeletal regulation, neurite elongation and branching, synaptic vesicles spatial localization, and synapses formation and maturation (see Fornasiero et al. (2010) for a review). To date, the role of the *SYN1* gene has been mostly studied *in vitro* on mouse hippocampal neurons, an approach that, while informative, does not allow a complete picture of the possible outcome of a mutation on the extremely complex neuronal development of the human brain. In this sense, this study represents the first observations of the effects of a *SYN1* mutation on cerebral microstructure *in vivo* in the mature human brain. It should be mentioned however that given our small sample size, it is hard to generalize our findings to a larger population of $SYN1_{Q555x}$ carriers. Nevertheless, it is interesting and informative to propose an interpretation of the observations made in our group of subjects.

The observations of altered diffusivity metrics points to changes in the cortical structure at the microscopic level, as opposed to changes in tissue composition, such as water or myelin content. Given that *SYN1* is known to be implicated in neuropil development, and that diffusion in the cortex is mostly restricted by the presence of neurites (Jespersen et al., 2012; Kleinnijenhuis et al., 2013; Leuze et al., 2014; Seehaus et al., 2015; Shepherd et al., 2007), we hypothesize that these observations are consistent with an increase in radial and/or tangential fiber population density (see Figure 14). This increase in the overall number of neurites would indeed impair the free diffusivity of water and increase the anisotropy, in the case where the radial population increase is greater than the tangential component increase (Figure 14c). This could be tentatively explained in different ways.

First, this could be the result of a cortical structure of smaller, thinner, and more densely packed neurites (Figure 14d). In this model, the

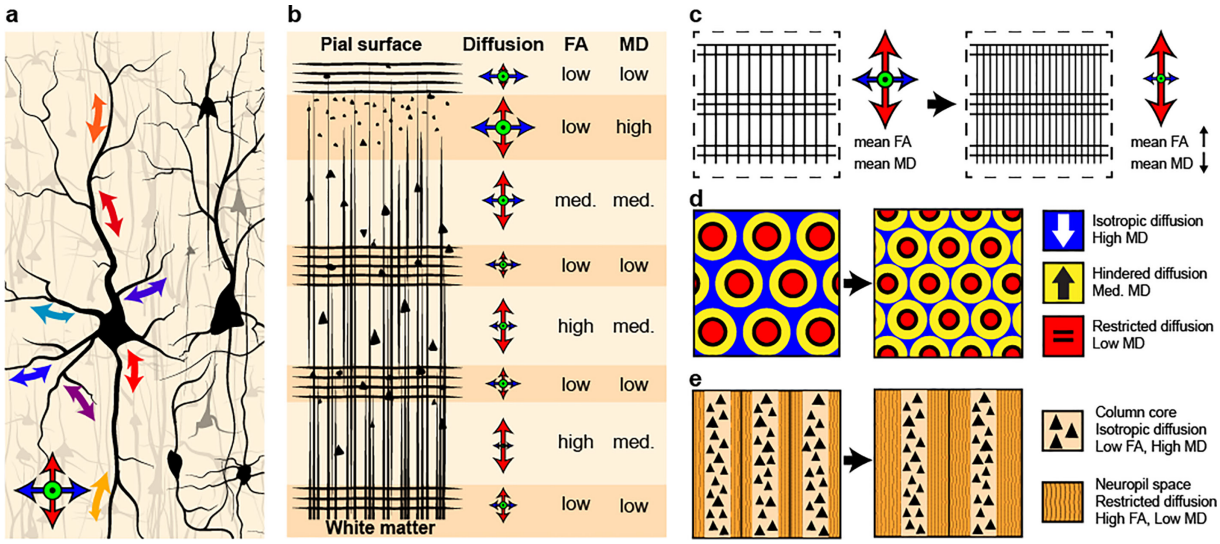

FIGURE 14 Microstructural interpretation of diffusion results. (a) On a microscopic (cellular) scale, diffusion in the cortex is complex. Water molecules movement is restricted by the presence of barriers, which are mainly cell membranes of myelinated or unmyelinated neurites. Given the dense and complex structure of cortical gray matter, the mean diffusivity is quite low and mostly isotropic. (b) On a mesoscopic scale, diffusion is found to be sensitive to the layered cortical structure of radial (perpendicular to the cortex surface) and tangential (parallel to the surface) fibers. (c) On a macroscopic scale, that is at the resolution of the MRI experiment, diffusion metrics represent an average over the full cortex thickness. Increased density of radial and/or tangential fiber populations in variable proportions could explain the increase in FA and decrease in MD observed in the $SYN1_{Q555X}$ group. (d) A three-compartment model demonstrates how a structure of thinner and more densely packed neurites can change various metrics, as observed in our data. In this model, ISOVF (in blue) is lowered, while ICVF (in red) is unchanged. The third compartment (=1 − (ISOVF + ICVF), in yellow) thus needs to increase. The increase in overall membrane surface area (black circles) increases the macromolecular protons fraction, which would lower the measurement of PD and T2*. (e) The increased population of neurites could also be explained by a model where the neurites morphology is unchanged, but occupy a larger volume fraction overall. In this model, the neuropil space is increased, which could be for example a result of increased space between minicolumn core, that is columns of dense cells soma. Assuming the NODDI intra-cellular volume fraction correctly estimates the space occupied by neurites, this model would lead to increased ICVF, which is not observed in our data. However, the NODDI model still needs validation in the cortex and in pathology, and assuming that ICVF truly represents neurites is risky [Color figure can be viewed at wileyonlinelibrary.com]

isotropic diffusion compartment (ISOVF) is decreased, while the intracellular volume fraction (ICVF) remains unchanged, as is observed in our data. This would also likely lower the fraction of free water protons (lower PD) and T2*, due to an increase in the overall cell membrane surface area. Another possible explanation could be that the cell morphology remains unchanged, but the ratio of somatic to neuropil volume fraction is lowered. For example, an arrangement of wider minicolumns driven by an increase in neuropil width is possible (Figure 14e). An alteration of cortical minicolumnar morphometry would agree with histological observations in the cortex of dyslexic and ASD subjects (Casanova, Buxhoeveden, Cohen, Switala, & Roy, 2002; Opris & Casanova, 2014). Finally, a denser arrangement of neurites would also presumably lead to increased local connectivity, which could in turn induce hyperexcitability, a defining feature of epilepsy. It is also plausible that this increase in neuropil volume fraction could be indicative of an increased number of fibers connecting the cortex to sub-cortical structures, as significant alterations in the right caudate nuclei and thalamus, both structures being highly connected to the cortex, were also observed (see Figure 13).

The presented model to explain diffusion data (reduced MD and increased FA) suggest increased density of radial and tangential fiber populations in the $SYN1_{Q555X}$ group. Although this may appear contradictory to *in vitro* observations suggesting impaired axon elongation, it should be kept in mind that results from studies conducted on primary cultures of hippocampal neurons from genetically altered mice should not prematurely be compared to *in vivo* neuroimaging observations. Indeed, histological analysis of brains derived from single and multiple synapsin knockouts have revealed broadly normal general structure and morphology (Chin et al., 1995; Gitler 2004; Takei et al., 1995), suggesting possible compensatory mechanisms which may occur in the human's complex environment but not in cultured neurons (Cesca et al., 2010). A delayed growth might occur *in vivo*, but could be corrected or even aberrantly overcorrected during development.

3.4.4 | Data processing

Every effort was made to ensure that each modality benefited from an optimal processing pipeline. It should be noted however that the use of various processing tools might have an impact on the results, to some extent. For example, omitting the Gibbs ringing removal in the diffusion data, or the denoising stage in the multi-contrast data processing could have hypothetically resulted in slightly different results. While we could have made the choice to reduce data processing to a minimum, we chose instead to optimize each processing pipeline to maximize data quality, and we believe this resulted in robust and reliable results.

3.4.5 | Diffusion models applicability in the cortex

Some studies have found that MK outperformed other diffusion metrics, such as MD and FA, as a measure of microstructural complexity, especially in white matter (Gao et al., 2012; Helpern et al., 2011; Umesh Rudrapatna et al., 2014; Zhu et al., 2015). While this increased sensitivity was the main reason to include MK in our study to begin with, our results showed that MK was less sensitive to detect changes in this case, and that MD was instead the most affected parameter. Furthermore, the suggested increased density of fiber populations in the $SYN1_{Q555x}$ group would suggest an increased complexity that should be expected to result in an increase in MK and ICVF. Therefore, our results do not seem to corroborate the proposed model in this regard. However, one should keep in mind that diffusion in the cortex is a very complex function of several physical and physiological parameters, and that unambiguously asserting specific causal relationships between tissue properties and MR diffusion parameters is very challenging. Thus, the suggested increase in fiber density remains a speculative and simplistic model at this point, and it is possible that other processes could in part explain our results. For example, changes in compartments permeability, cell shape or cell population sizes, could affect the diffusion measures in a non-trivial manner, affecting MD/ISOVF more than MK/ICVF in this particular situation. Another interesting possibility is that MK/ICVF could be mostly representative of myelinated axons (Fukutomi et al., 2018), thus suggesting an increase only in unmyelinated dendrites density in the $SYN1_{Q555x}$ population. It is also plausible that the behavior of MK/ICVF differs between the gray matter and the white matter, and thus that its interpretation may not be directly transferable from what is known in the white matter to the gray matter, where its properties are not as well established. For example, Falangola et al. (2008) have studied the patterns of MK, MD, and FA changes with age (from age 13 to 85 years) in the prefrontal cortex. They have found that mean MK values increased with age in the GM, while it decreased with age in the WM. The MK increase with age in GM was also observed in our data, as shown in Figure 12. Therefore, it appears that in GM, MK might not be entirely representative of neurites complexity, as it is not likely to increase with age, but on the contrary probably slightly decreases (Hof & Morrison, 2004; Pannese, 2011; Petralia, Mattson, & Yao, 2014).

Given the increasingly diverse amount of biophysical model to explain diffusion signal, one may question the effect of choosing one particular model over another, as such a choice may possibly be a confounding factor in the results obtained. While we are aware that the validity of NODDI is still debated, given its limitation due to the various assumptions underpinning the model (fixed diffusivities, impermeable neurites, tortuosity model), we chose to still include it in our study for several reasons. First, while the interpretation of its metrics cannot be taken for granted, it has been shown to be sensitive to detect microstructural changes, even in gray matter (e.g., Granberg et al., 2017; Kamagata et al., 2017; Nazeri et al., 2017). Secondly, the inclusion of a larger number of metrics is desirable in the NPC framework, as it serves to increase the overall sensitivity, even given the redundancy between both diffusion models. Finally, we believe that adding our results to the growing pool of literature might serve for future studies especially looking to resolve these models' validity in the cortex. As such, our results on across-cortex parametric correlation represents an interesting starting point that might trigger additional research.

As a further validation to exclude the choice of diffusion model as a confounding factor, we applied the recently proposed "multi compartment microscopic diffusion model" by Kaden et al. (2016). This model relaxes some of the constraints imposed in the NODDI model, and allows the estimation of the intrinsic diffusivity (Dint) and intra-neurite volume fraction (Vint). Using this model, we found results that are essentially the same as with DKI or NODDI (see Supporting Information). Thus, it appears that, at least in the present study, the choice of a particular diffusion model does not alter the observations significantly, and that the main conclusions of our study remain unchanged.

We must nonetheless warn the reader with regards to the interpretation of the results presented in this study. While we chose to include a biophysical model of the diffusion signal with the objective of aiming for increased specificity, the lack of a thorough validation of these models implies that their interpretation remains speculative. The proposed model we tentatively put forward thus remains hypothetical at this point, and should not be regarded as a definitive conclusion, but only as one plausible possibility. One should not however use these results as a conclusive validation of any biophysical model of diffusion signal, be it NODDI or any other model.

4 | CONCLUSION

We investigated the impacts of the $SYN1_{Q555x}$ mutation on cortical microstructure using DKI, NODDI, T1, T2*, and PD mapping. Using a surface-based analysis approach, we observed alterations in 13 mutation carriers relative to 13 age- and sex-matched controls in a predominantly right hemispheric network. In summary, the altered regions were found to have some general characteristics: MD/ISOVF significantly decreased, FA significantly increased, no changes in ICVF, OD, and MK variables across regions, T1 increased but not significantly, T2* decreased but not significantly, and PD significantly decreased.

In conclusion, this study is the first to use diffusion imaging and quantitative multiparametric mapping successfully in a surface-based approach to detect cortical anomalies in a group of subjects with a well-defined genotype, linked to language impairments, epilepsy and ASD. Microstructural alterations were found in several regions usually involved in oral and written language as well as dyslexia. The most significant changes in these regions were lowered MD and increased FA in $SYN1_{Q555x}$ subjects, suggesting an increase in neuropil density or volume fraction.

Although the results are difficult to generalize to a wider population, this study shows that surface-based diffusion MRI can effectively be used to characterize subtle cortical pathology not detectable otherwise, even when only a relatively small group of subjects is available. We hope the unique results we presented here will encourage more research groups to use this promising method.

ACKNOWLEDGMENTS

This study was funded in part by the Quebec Bio-Imaging Network (QBIN) pilot project grant number 13.19 and by the Savoy Foundation for epilepsy.

CONFLICT OF INTEREST

Guillaume Gilbert receives salary from Philips Healthcare for work outside of the scope of this study.

ORCID

Jean-François Cabana http://orcid.org/0000-0003-0579-5378

REFERENCES

Andersson, J. L. R., Skare, S., & Ashburner, J. (2003). How to correct susceptibility distortions in spin-echo echo-planar images: Application to diffusion tensor imaging. *NeuroImage*, *20*(2), 870–888. https://doi.org/10.1016/S1053-8119(03)00336-7

Andersson, J. L. R., & Sotiropoulos, S. N. (2015). An integrated approach to correction for off-resonance effects and subject movement in diffusion MR imaging. *NeuroImage*, *125*, 1063–1078. https://doi.org/10.1016/j.neuroimage.2015.10.019

Bailey, S., Hoeft, F., Aboud, K., & Cutting, L. (2016). Anomalous gray matter patterns in specific reading comprehension deficit are independent of dyslexia. *Annals of Dyslexia*, *66*(3), 256–274. https://doi.org/10.1007/s11881-015-0114-y

Baillieux, H., Vandervliet, E. J. M., Manto, M., Parizel, P. M., Deyn, P. P. D., & Mariën, P. (2009). Developmental dyslexia and widespread activation across the cerebellar hemispheres. *Brain and Language*, *108*(2), 122–132. https://doi.org/10.1016/j.bandl.2008.10.001

Barquero, L. A., Davis, N., Cutting, L. E., Tolvanen, A., & Lyytinen, H. (2014). Neuroimaging of reading intervention: A systematic review and activation likelihood estimate meta-analysis. *PLoS ONE*, *9*(1), e83668. https://doi.org/10.1371/journal.pone.0083668

Bernhardt, B. C, Bernasconi, N., Concha, L, & Bernasconi, A. (2010). Cortical thickness analysis in temporal lobe epilepsy Reproducibility and relation to outcome. *Neurology*, *74*(22), 1776–1784.

Billiet, T., Vandenbulcke, M., Mädler, B., Peeters, R., Dhollander, T., Zhang, H., … Emsell, L. (2015). Age-related microstructural differences quantified using myelin water imaging and advanced diffusion MRI. *Neurobiology of Aging*, *36*(6), 2107–2121. https://doi.org/10.1016/j.neurobiolaging.2015.02.029

Boisgueheneuc, F. D., Levy, R., Volle, E., Seassau, M., Duffau, H., Kinkingnehun, S., … Dubois, B. (2006). Functions of the left superior frontal gyrus in humans: A lesion study. *Brain*, *129*(12), 3315–3328. https://doi.org/10.1093/brain/awl244

Bonilha, L., Lee, C.-Y., Jensen, J. H., Tabesh, A., Spampinato, M. V., Edwards, J. C., … Helpern, J. A. (2015). Altered microstructure in temporal lobe epilepsy: A diffusional kurtosis imaging study. *American Journal of Neuroradiology*, *36*(4), 719–724. https://doi.org/10.3174/ajnr.A4185

Bullmore, E. T., Suckling, J., Overmeyer, S., Rabe-Hesketh, S., Taylor, E., & Brammer, M. J. (1999). Global, voxel, and cluster tests, by theory and permutation, for a difference between two groups of structural MR images of the brain. *IEEE Transactions on Medical Imaging*, *18*(1), 32–42. https://doi.org/10.1109/42.750253

Cain, K. (2006). Individual differences in children's memory and reading comprehension: An investigation of semantic and inhibitory deficits. *Memory*, *14*(5), 553–569. https://doi.org/10.1080/09658210600624481

Carretti, B., Borella, E., Cornoldi, C., & De Beni, R. (2009). Role of working memory in explaining the performance of individuals with specific reading comprehension difficulties: A meta-analysis. *Learning and Individual Differences*, *19*(2), 246. https://doi.org/10.1016/j.lindif.2008.10.002

Casanova, M. F., Buxhoeveden, D. P., Cohen, M., Switala, A. E., & Roy, E. L. (2002). Minicolumnar pathology in dyslexia. *Annals of Neurology*, *52*(1), 108–110. https://doi.org/10.1002/ana.10226

Caverzasi, E., Papinutto, N., Castellano, A., Zhu, A. H., Scifo, P., Riva, M., … Henry, R. G. (2016). Neurite orientation dispersion and density imaging color maps to characterize brain diffusion in neurologic disorders. *Journal of Neuroimaging*, 1–5. https://doi.org/10.1111/jon.12359

Caylak, E. (2009). Neurobiological approaches on brains of children with dyslexia. *Review. Academic Radiology*, *16*(8), 1003–1024. https://doi.org/10.1016/j.acra.2009.02.012

Cesca, F., Baldelli, P., Valtorta, F., & Benfenati, F. (2010). The synapsins: Key actors of synapse function and plasticity. *Progress in Neurobiology*, *91*(4), 313–348. https://doi.org/10.1016/j.pneurobio.2010.04.006

Chin, L. S., Li, L., Ferreira, A., Kosik, K. S., & Greengard, P. (1995). Impairment of axonal development and of synaptogenesis in hippocampal neurons of synapsin I-deficient mice. *Proceedings of the National Academy of Sciences of the United States of America*, *92*(20), 9230–9234. https://doi.org/10.1073/pnas.92.20.9230

Cohen-Adad, J. (2014). What can we learn from T2* maps of the cortex?. *NeuroImage*, *93*, 189–200. https://doi.org/10.1016/j.neuroimage.2013.01.023

Cui, Z., Xia, Z., Su, M., Shu, H., & Gong, G. (2016). Disrupted white matter connectivity underlying developmental dyslexia: A machine learning approach. *Human Brain Mapping*, *37*(4), 1443–1458. https://doi.org/10.1002/hbm.23112

Daducci, A., Canales-Rodríguez, E. J., Zhang, H., Dyrby, T. B., Alexander, D. C., & Thiran, J.-P. (2015). Accelerated Microstructure Imaging via Convex Optimization (AMICO) from diffusion MRI data. *NeuroImage*, *105*, 32–44. https://doi.org/10.1016/j.neuroimage.2014.10.026

Elnakib, A., Soliman, A., Nitzken, M., Casanova, M. F., Gimel'farb, G., & El-Baz, A. (2014). Magnetic resonance imaging findings for dyslexia: A review. *Journal of Biomedical Nanotechnology*, *10*(10), 2778–2805. https://doi.org/10.1166/jbn.2014.1895

Falangola, M. F., Jensen, J. H., Babb, J. S., Hu, C., Castellanos, F. X., Di Martino, A., … Helpern, J. A. (2008). Age-related non-Gaussian diffusion patterns in the prefrontal brain. *Journal of Magnetic Resonance Imaging*, *28*(6), 1345–1350. https://doi.org/10.1002/jmri.21604

Farmer, M. E., & Klein, R. M. (1995). The evidence for a temporal processing deficit linked to dyslexia: A review. *Psychonomic Bulletin & Review*, *2*(4), 460–493. https://doi.org/10.3758/BF03210983

Fassio, A., Patry, L., Congia, S., Onofri, F., Piton, A., Gauthier, J., … Cossette, P. (2011). SYN1 loss-of-function mutations in autism and partial epilepsy cause impaired synaptic function. *Human Molecular Genetics*, *20*(12), 2297–2307. https://doi.org/10.1093/hmg/ddr122

Finn, E. S., Shen, X., Holahan, J. M., Scheinost, D., Lacadie, C., Papademetris, X., … Constable, R. T. (2014). Disruption of functional networks in dyslexia: A whole-brain, data-driven analysis of connectivity. *Biological Psychiatry*, *76*(5), 397–404. https://doi.org/10.1016/j.biopsych.2013.08.031

Fischl, B. (2004). Automatically parcellating the human cerebral cortex. *Cerebral Cortex*, *14*(1), 11–22. https://doi.org/10.1093/cercor/bhg087

Fornasiero, E. F., Bonanomi, D., Benfenati, F., & Valtorta, F. (2010). The role of synapsins in neuronal development. *Cellular and Molecular Life Sciences*, *67*(9), 1383–1396. https://doi.org/10.1007/s00018-009-0227-8

Frye, R. E., Liederman, J., Hasan, K. M., Lincoln, A., Malmberg, B., McLean, J., & Papanicolaou, A. (2011). Diffusion tensor quantification of the relations between microstructural and macrostructural indices of white matter and reading. *Human Brain Mapping*, *32*(8), 1220–1235. https://doi.org/10.1002/hbm.21103

Fukutomi, H., Glasser, M. F., Zhang, H., Autio, J. A., Coalson, T. S., Okada, T., … Hayashi, T. (2018). Neurite imaging reveals microstructural variations in human cerebral cortical gray matter. *NeuroImage*, https://doi.org/10.1016/j.neuroimage.2018.02.017

Galaburda, A. M., LoTurco, J., Ramus, F., Fitch, R. H., & Rosen, G. D. (2006). From genes to behavior in developmental dyslexia. *Nature Neuroscience*, *9*(10), 1213–1217. https://doi.org/10.1038/nn1772

Gao, Y., Zhang, Y., Wong, C.-S., Wu, P.-M., Zhang, Z., Gao, J., … Huang, B. (2012). Diffusion abnormalities in temporal lobes of children with temporal lobe epilepsy: A preliminary diffusional kurtosis imaging study and comparison with diffusion tensor imaging. *NMR in Biomedicine*, *25*(12), 1369–1377. https://doi.org/10.1002/nbm.2809

Garcia, C. C., Blair, H. J., Seager, M., Coulthard, A., Tennant, S., Buddles, M., … Goodship, J. A. (2004). Identification of a mutation in synapsin I, a synaptic vesicle protein, in a family with epilepsy. *Journal of Medical Genetics*, *41*(3), 183–186. https://doi.org/10.1136/jmg.2003.013680

Gelman, N., Ewing, J. R., Gorell, J. M., Spickler, E. M., & S, E. G. (2013). Interregional variation of longitudinal relaxation rates in human brain at 3.0 T: Relation to estimated iron and water contents. *NeuroImage*, *44*(1), 137–141. https://doi.org/10.1016/j.neuroimage.2009.09.037

Geschwind, D. H. (2011). Genetics of autism spectrum disorders. *Trends in Cognitive Sciences*, *15*(9), 409–416. https://doi.org/10.1016/j.tics.2011.07.003

Gitler, D. (2004). Different presynaptic roles of synapsins at excitatory and inhibitory synapses. *Journal of Neuroscience*, *24*(50), 11368–11380. https://doi.org/10.1523/JNEUROSCI.3795-04.2004

Glasser, M. F., Smith, S. M., Marcus, D. S., Andersson, J. L. R., Auerbach, E. J., Behrens, T. E. J., … Van Essen, D. C. (2016). The Human Connectome Project's neuroimaging approach. *Nature Neuroscience*, *19*(9), 1175–1187. https://doi.org/10.1038/nn.4361

Glasser, M. F., Sotiropoulos, S. N., Wilson, J. A., Coalson, T. S., Fischl, B., Andersson, J. L., … Jenkinson, M. (2013). The minimal preprocessing pipelines for the Human Connectome Project. *NeuroImage*, *80*, 105–124. https://doi.org/10.1016/j.neuroimage.2013.04.127

Granberg, T., Fan, Q., Treaba, C. A., Ouellette, R., Herranz, E., Mangeat, G., … Mainero, C. (2017). In vivo characterization of cortical and white matter neuroaxonal pathology in early multiple sclerosis. *Brain*, *140*(11), 2912–2926. https://doi.org/10.1093/brai/awx247

Grinberg, F., Maximov, I. I., Farrher, E., Neuner, I., Amort, L., Thönneßen, H., … Shah, N. J. (2016). Diffusion kurtosis metrics as biomarkers of microstructural development: A comparative study of a group of children and a group of adults. *NeuroImage*, (*October 2015*), 0–1. https://doi.org/10.1016/j.neuroimage.2016.08.033

Guglielmetti, C., Veraart, J., Roelant, E., Mai, Z., Daans, J., Van Audekerke, J., … Verhoye, M. (2016). Diffusion kurtosis imaging probes cortical alterations and white matter pathology following cuprizone induced demyelination and spontaneous remyelination. *NeuroImage*, *125*, 363–377. https://doi.org/10.1016/j.neuroimage.2015.10.052

Helpern, J. A., Adisetiyo, V., Falangola, M. F., Hu, C., Di Martino, A., Williams, K., … Jensen, J. H. (2011). Preliminary evidence of altered gray and white matter microstructural development in the frontal lobe of adolescents with attention-deficit hyperactivity disorder: A diffusional kurtosis imaging study. *Journal of Magnetic Resonance Imaging*, *33*(1), 17–23. https://doi.org/10.1002/jmri.22397

Hof, P. R., & Morrison, J. H. (2004). The aging brain: Morphomolecular senescence of cortical circuits. *Trends in Neurosciences*, *27*(10), 607–613. https://doi.org/10.1016/J.TINS.2004.07.013

Hu, W. F., Chahrour, M. H., & Walsh, C. A. (2014). The diverse genetic landscape of neurodevelopmental disorders. *Annual Review of Genomics and Human Genetics*, *15*(1), 195–213. https://doi.org/10.1146/annurev-genom-090413-025600

Jenkinson, M., Bannister, P., Brady, M., & Smith, S. (2002). Improved optimization for the robust and accurate linear registration and motion correction of brain images. *NeuroImage*, *17*(2), 825–841. Retrieved from http://www.ncbi.nlm.nih.gov/pubmed/12377157

Jensen, J. H., & Helpern, J. A. (2010). MRI quantification of non-Gaussian water diffusion by kurtosis analysis. *NMR in Biomedicine*, *23*(7), 698–710. https://doi.org/10.1002/nbm.1518

Jespersen, S. N., Leigland, L. A., Cornea, A., & Kroenke, C. D. (2012). Determination of axonal and dendritic orientation distributions within the developing cerebral cortex by diffusion tensor imaging. *IEEE Transactions on Medical Imaging*, *31*(1), 16–32. https://doi.org/10.1109/TMI.2011.2162099

Jutras, J. D., Wachowicz, K., Gilbert, G., & De Zanche, N. (2017). SNR efficiency of combined bipolar gradient echoes: Comparison of three-dimensional FLASH, MPRAGE, and multiparameter mapping with VFA-FLASH and MP2RAGE. *Magnetic Resonance in Medicine*, *77*(6), 2186–2202. https://doi.org/10.1002/mrm.26306

Kaden, E., Kelm, N. D., Carson, R. P., Does, M. D., & Alexander, D. C. (2016). Multi-compartment microscopic diffusion imaging. *NeuroImage*, *139*, 346–359. https://doi.org/10.1016/j.neuroimage.2016.06.002

Kamagata, K., Zalesky, A., Hatano, T., Ueda, R., Di Biase, M. A., Okuzumi, A., … Aoki, S. (2017). Gray matter abnormalities in idiopathic Parkinson's disease: Evaluation by diffusional kurtosis imaging and neurite orientation dispersion and density imaging. *Human Brain Mapping*, *3722*(December 2016), 3704–3722. https://doi.org/10.1002/hbm.23628

Kellner, E., Dhital, B., Kiselev, V. G., & Reisert, M. (2015). Gibbs-ringing artifact removal based on local subvoxel-shifts. *Magnetic Resonance in Medicine*, *0*(October), n/a-n/a. https://doi.org/10.1002/mrm.26054

Kleinnijenhuis, M., Zerbi, V., Küsters, B., Slump, C. H., Barth, M., & van Cappellen van Walsum, A.-M. (2013). Layer-specific diffusion weighted imaging in human primary visual cortex in vitro. *Cortex*, *49*(9), 2569–2582. https://doi.org/10.1016/j.cortex.2012.11.015

Kunz, N., Zhang, H., Vasung, L., O'Brien, K. R., Assaf, Y., Lazeyras, F., … Hüppi, P. S. (2014). Assessing white matter microstructure of the newborn with multi-shell diffusion MRI and biophysical compartment models. *NeuroImage*, *96*, 288–299. https://doi.org/10.1016/j.neuroimage.2014.03.057

Lanzafame, S., Giannelli, M., Garaci, F., Floris, R., Duggento, A., Guerrisi, M., & Toschi, N. (2016). Differences in Gaussian diffusion tensor imaging and non-Gaussian diffusion kurtosis imaging model-based estimates of diffusion tensor invariants in the human brain. *Medical Physics*, *43*(5), 2464. https://doi.org/10.1118/1.4946819

Lebel, C., Shaywitz, B., Holahan, J., Shaywitz, S., Marchione, K., & Beaulieu, C. (2013). Diffusion tensor imaging correlates of reading ability in dysfluent and non-impaired readers. *Brain and Language*, *125*(2), 215–222. https://doi.org/10.1016/j.bandl.2012.10.009

Lee, C. Y., Tabesh, A., Spampinato, M. V., Helpern, J. A., Jensen, J. H., & Bonilha, L. (2014). Diffusional kurtosis imaging reveals a distinctive pattern of microstructural alternations in idiopathic generalized

epilepsy. *Acta Neurologica Scandinavica*, *130*(3), 148–155. https://doi.org/10.1111/ane.12257

Leuze, C. W. U., Anwander, A., Bazin, P.-L., Dhital, B., Stuber, C., Reimann, K., … Turner, R. (2014). Layer-specific intracortical connectivity revealed with diffusion MRI. *Cerebral Cortex*, *24*(2), 328–339. https://doi.org/10.1093/cercor/bhs311

Lewis, D. A., & Levitt, P. (2002). Schizophrenia as a disorder of neurodevelopment. *Annual Review of Neuroscience*, *25*(1), 409–432. https://doi.org/10.1146/annurev.neuro.25.112701.142754

Lignani, G., Raimondi, A., Ferrea, E., Rocchi, A., Paonessa, F., Cesca, F., … Benfenati, F. (2013). Epileptogenic Q555X SYN1 mutant triggers imbalances in release dynamics and short-term plasticity. *Human Molecular Genetics*, *22*(11), 2186–2199. https://doi.org/10.1093/hmg/ddt071

Lu, H., Jensen, J. H., Ramani, A., & Helpern, J. A. (2006). Three-dimensional characterization of non-gaussian water diffusion in humans using diffusion kurtosis imaging. *NMR in Biomedicine*, *19*(2), 236–247. https://doi.org/10.1002/nbm.1020

Lutti, A., Dick, F., Sereno, M. I., & Weiskopf, N. (2014). Using high-resolution quantitative mapping of R1 as an index of cortical myelination. *NeuroImage*, *93*, 176–188. https://doi.org/10.1016/j.neuroimage.2013.06.005

Maisog, J. M., Einbinder, E. R., Flowers, D. L., Turkeltaub, P. E., & Eden, G. F. (2008). A meta-analysis of functional neuroimaging studies of dyslexia. *Annals of the New York Academy of Sciences*, *1145*(1), 237–259. https://doi.org/10.1196/annals.1416.024

Manjón, J. V., & Coupé, P. (2016). volBrain: An online MRI brain volumetry system. *Frontiers in Neuroinformatics*, *10*, 30. https://doi.org/10.3389/fninf.2016.00030

Manjón, J. V., Coupé, P., Martí-Bonmatí, L., Collins, D. L., & Robles, M. (2010). Adaptive non-local means denoising of MR images with spatially varying noise levels. *Journal of Magnetic Resonance Imaging*, *31*(1), 192–203. https://doi.org/10.1002/jmri.22003

Mueller, B. A., Lim, K. O., Hemmy, L., & Camchong, J. (2015). Diffusion MRI and its Role in neuropsychology. *Neuropsychology Review*, https://doi.org/10.1007/s11065-015-9291-z

Nazeri, A., Mulsant, B. H., Rajji, T. K., Levesque, M. L., Pipitone, J., Stefanik, L., … Voineskos, A. N. (2017). Gray matter neuritic microstructure deficits in schizophrenia and bipolar disorder. *Biological Psychiatry*, *82*(10), 726–736. https://doi.org/10.1016/j.biopsych.2016.12.005

Nguyen, D. K., Rouleau, I., Senechal, G., Ansaldo, A. I., Gravel, M., Benfenati, F., … Cossette, P. (2015). X-linked focal epilepsy with reflex bathing seizures: Characterization of a distinct epileptic syndrome. *Epilepsia*, *56*(7), 1098–1108. https://doi.org/10.1111/epi.13042

Opris, I., & Casanova, M. F. (2014). Prefrontal cortical minicolumn: From executive control to disrupted cognitive processing. *Brain*, *137*(7), 1863–1875. https://doi.org/10.1093/brain/awt359

Pagnamenta, A. T., Bacchelli, E., de Jonge, M. V., Mirza, G., Scerri, T. S., Minopoli, F., … Monaco, A. P. (2010). Characterization of a family with rare deletions in CNTNAP5 and DOCK4 suggests novel risk loci for autism and dyslexia. *Biological Psychiatry*, *68*(4), 320–328. https://doi.org/10.1016/j.biopsych.2010.02.002

Pannese, E. (2011). Morphological changes in nerve cells during normal aging. *Brain Structure and Function*, *216*(2), 85–89. https://doi.org/10.1007/s00429-011-0308-y

Paulesu, E., Danelli, L., & Berlingeri, M. (2014). Reading the dyslexic brain: Multiple dysfunctional routes revealed by a new meta-analysis of PET and fMRI activation studies. *Frontiers in Human Neuroscience*, *8*, 830. https://doi.org/10.3389/fnhum.2014.00830

Perrone, D., Aelterman, J., Pizurica, A., Jeurissen, B., Philips, W., & Leemans, A. (2015). The effect of Gibbs ringing artifacts on measures derived from diffusion MRI. *NeuroImage*, *120*, 441–455. https://doi.org/10.1016/j.neuroimage.2015.06.068

Petralia, R. S., Mattson, M. P., & Yao, P. J. (2014). Communication breakdown: The impact of ageing on synapse structure. *Ageing Research Reviews*, *14*, 31–42. https://doi.org/10.1016/J.ARR.2014.01.003

Pollack, C., Luk, G., & Christodoulou, J. A. (2015). A meta-analysis of functional reading systems in typically developing and struggling readers across different alphabetic languages. *Frontiers in Psychology*, *6*, 191. https://doi.org/10.3389/fpsyg.2015.00191

Price, C. J. (2012). A review and synthesis of the first 20years of PET and fMRI studies of heard speech, spoken language and reading. *NeuroImage*, *62*(2), 816–847. https://doi.org/10.1016/j.neuroimage.2012.04.062

Richardson, A. J., & Ross, M. A. (2000). Fatty acid metabolism in neurodevelopmental disorder: A new perspective on associations between attention-deficit/hyperactivity disorder, dyslexia, dyspraxia and the autistic spectrum. *Prostaglandins, Leukotrienes, and Essential Fatty Acids*, *63*(1–2), 1–9. https://doi.org/10.1054/plef.2000.0184

Richlan, F., Kronbichler, M., & Wimmer, H. (2009). Functional abnormalities in the dyslexic brain: A quantitative meta-analysis of neuroimaging studies. *Human Brain Mapping*, *30*(10), 3299–3308. https://doi.org/10.1002/hbm.20752

Richlan, F., Kronbichler, M., & Wimmer, H. (2011). Meta-analyzing brain dysfunctions in dyslexic children and adults. *NeuroImage*, *56*(3), 1735–1742. https://doi.org/10.1016/j.neuroimage.2011.02.040

Rimrodt, S. L., Clements-Stephens, A. M., Pugh, K. R., Courtney, S. M., Gaur, P., Pekar, J. J., & Cutting, L. E. (2009). Functional MRI of sentence comprehension in children with dyslexia: Beyond word recognition. *Cerebral Cortex*, *19*(2), 402–413. https://doi.org/10.1093/cercor/bhn092

Rimrodt, S. L., Peterson, D. J., Denckla, M. B., Kaufmann, W. E., & Cutting, L. E. (2010). White matter microstructural differences linked to left perisylvian language network in children with dyslexia. *Cortex*, *46*(6), 739–749. https://doi.org/10.1016/j.cortex.2009.07.008

Rossignol, E. (2011). Genetics and function of neocortical GABAergic interneurons in neurodevelopmental disorders. *Neural Plasticity*, *2011*, 1. https://doi.org/10.1155/2011/649325

Schachter, S. C., Galaburda, A. M., & Ransil, B. J. (1993). A history of dyslexia in patients with epilepsy: Clinical associations. *Journal of Epilepsy*, *6*(4), 267–271. https://doi.org/10.1016/0896-6974(93)90012-Y

Seehaus, A., Roebroeck, A., Bastiani, M., Fonseca, L., Bratzke, H., Lori, N., … Galuske, R.. (2015). Histological validation of high-resolution DTI in human post mortem tissue. *Frontiers in Neuroanatomy*, *9*(July), 98. https://doi.org/10.3389/fnana.2015.00098

Shaywitz, S. E., Shaywitz, B. A., Author, A. (2008). Paying attention to reading: The neurobiology of reading and dyslexia. *Development and Psychopathology*, *20*(04), 1329–1349. https://doi.org/10.1017/S0954579408000631

Shepherd, T. M., Özarslan, E., Yachnis, A. T., King, M. A., & Blackband, S. J. (2007). Diffusion tensor microscopy indicates the cytoarchitectural basis for diffusion anisotropy in the human hippocampus. *American Journal of Neuroradiology*, *28*(5), 958–964.

Smith, S. M. (2002). Fast robust automated brain extraction. *Human Brain Mapping*, *17*(3), 143–155. https://doi.org/10.1002/hbm.10062

Smith, S. M., Jenkinson, M., Woolrich, M. W., Beckmann, C. F., Behrens, T. E. J., Johansen-Berg, H., … Matthews, P. M. (2004). Advances in functional and structural MR image analysis and implementation as FSL. *NeuroImage*, *23*(Suppl. 1), S208–S219. https://doi.org/10.1016/j.neuroimage.2004.07.051

Steven, A. J., Zhuo, J., & Melhem, E. R. (2014). Diffusion kurtosis imaging: An emerging technique for evaluating the microstructural environment of the brain. *American Journal of Roentgenology*, *202*(1), W26–W33. https://doi.org/10.2214/AJR.13.11365

Stüber, C., Morawski, M., Schäfer, A., Labadie, C., Wähnert, M., Leuze, C., … Turner, R. (2014). Myelin and iron concentration in the human brain: A quantitative study of MRI contrast. *NeuroImage*, *93*(P1), 95–106. https://doi.org/10.1016/j.neuroimage.2014.02.026

Takei, Y., Harada, A., Takeda, S., Kobayashi, K., Terada, S., Noda, T., … Hirokawa, N. (1995). Synapsin I deficiency results in the structural change in the presynaptic terminals in the murine nervous system. *Journal of Cell Biology*, *131*(6), 1789–1800. https://doi.org/10.1083/jcb.131.6.1789

Tamboer, P., Scholte, H. S., & Vorst, H. C. M. (2015). Dyslexia and voxel-based morphometry: Correlations between five behavioural measures of dyslexia and gray and white matter volumes. *Annals of Dyslexia*, *65*(3), 121–141. https://doi.org/10.1007/s11881-015-0102-2

Tuchman, R., Moshé, S. L., & Rapin, I. (2009). Convulsing toward the pathophysiology of autism. *Brain and Development*, *31*(2), 95–103. https://doi.org/10.1016/j.braindev.2008.09.009

Tuchman, R., & Rapin, I. (2002). Epilepsy in autism. *Lancet Neurology*, *1*(6), 352–358. https://doi.org/10.1016/S1474-4422(02)00160-6

Tustison, N. J., Avants, B. B., Cook, P. A., Zheng, Y., Egan, A., Yushkevich, P. A., & Gee, J. C. (2010). N4ITK: Improved N3 bias correction. *IEEE Transactions on Medical Imaging*, *29*(6), 1310–1320. https://doi.org/10.1109/TMI.2010.2046908

Umesh Rudrapatna, S., Wieloch, T., Beirup, K., Ruscher, K., Mol, W., Yanev, P., … Dijkhuizen, R. M. (2014). Can diffusion kurtosis imaging improve the sensitivity and specificity of detecting microstructural alterations in brain tissue chronically after experimental stroke? Comparisons with diffusion tensor imaging and histology. *NeuroImage*, *97*, 363–373. https://doi.org/10.1016/j.neuroimage.2014.04.013

Valdois, S., Bosse, M.-L., & Tainturier, M.-J. (2004). The cognitive deficits responsible for developmental dyslexia: Review of evidence for a selective visual attentional disorder. *Dyslexia*, *10*(4), 339–363. https://doi.org/10.1002/dys.284

Van Essen, D. C., Glasser, M. F., Dierker, D. L., Harwell, J., & Coalson, T. (2012). Parcellations and hemispheric asymmetries of human cerebral cortex analyzed on surface-based atlases. *Cerebral Cortex*, *22*(10), 2241–2262. https://doi.org/10.1093/cercor/bhr291

Veraart, J., Fieremans, E., Jelescu, I. O., Knoll, F., & Novikov, D. S. (2015). Gibbs ringing in diffusion MRI. *Magnetic Resonance in Medicine*, *0*. https://doi.org/10.1002/mrm.25866

Veraart, J., Fieremans, E., & Novikov, D. S. (2015). Diffusion MRI noise mapping using random matrix theory. *Magnetic Resonance in Medicine*, *0*, n/a-n/a. https://doi.org/10.1002/mrm.26059

Veraart, J., Novikov, D. S., Christiaens, D., Ades-Aron, B., Sijbers, J., & Fieremans, E. (2016). Denoising of diffusion MRI using random matrix theory. *NeuroImage*, *142*, 394–406. https://doi.org/10.1016/j.neuroimage.2016.08.016

Veraart, J., Poot, D. H. J., Van Hecke, W., Blockx, I., Van der Linden, A., Verhoye, M., & Sijbers, J. (2011). More accurate estimation of diffusion tensor parameters using diffusion Kurtosis imaging. *Magnetic Resonance in Medicine*, *65*(1), 138–145. https://doi.org/10.1002/mrm.22603

Veraart, J., Sijbers, J., Sunaert, S., Leemans, A., & Jeurissen, B. (2013). Weighted linear least squares estimation of diffusion MRI parameters: Strengths, limitations, and pitfalls. *NeuroImage*, *81*, 335–346. https://doi.org/10.1016/j.neuroimage.2013.05.028

Waldie, K. E., Wilson, A. J., Roberts, R., & Moreau, D. (2017). Reading network in dyslexia: Similar, yet different. *Brain and Language*, *174*, 29–41. https://doi.org/10.1016/j.bandl.2017.07.004

Walsh, T., McClellan, J. M., McCarthy, S. E., Addington, A. M., Pierce, S. B., Cooper, G. M., … Sebat, J. (2008). Rare structural variants disrupt multiple genes in neurodevelopmental pathways in schizophrenia. *Science (New York, N.Y.)*, *320*(5875), 539–543. https://doi.org/10.1126/science.1155174

Winkler, A. M., Ridgway, G. R., Webster, M. A., Smith, S. M., & Nichols, T. E. (2014). Permutation inference for the general linear model. *NeuroImage*, *92*, 381–397. https://doi.org/10.1016/j.neuroimage.2014.01.060

Winkler, A. M., Webster, M. A., Brooks, J. C., Tracey, I., Smith, S. M., & Nichols, T. E. (2016). Non-parametric combination and related permutation tests for neuroimaging. *Human Brain Mapping*, *37*(4), 1486–1511. https://doi.org/10.1002/hbm.23115

Winston, G. P. (2015). The potential role of novel diffusion imaging techniques in the understanding and treatment of epilepsy. *Quantitative Imaging in Medicine and Surgery*, *5*(2), 279–287. https://doi.org/10.3978/j.issn.2223-4292.2015.02.03

Winston, G. P., Micallef, C., Symms, M. R., Alexander, D. C., Duncan, J. S., & Zhang, H. (2014). Advanced diffusion imaging sequences could aid assessing patients with focal cortical dysplasia and epilepsy. *Epilepsy Research*, *108*(2), 336–339. https://doi.org/http://dx.doi.org/10.1016/j.eplepsyres.2013.11.004

Yan, X. U., Zhou, M., Ying, L., Yin, D., Fan, M., Yang, G., … Xu, D. (2013). Evaluation of optimized b-value sampling schemas for diffusion kurtosis imaging with an application to stroke patient data. *Computerized Medical Imaging and Graphics*, *37*(4), 272–280. https://doi.org/10.1016/j.compmedimag.2013.04.007

Zhang, H., Schneider, T., Wheeler-Kingshott, C. A., & Alexander, D. C. (2012). NODDI: Practical in vivo neurite orientation dispersion and density imaging of the human brain. *Neuroimage*, *61*(4), 1000–1016. https://doi.org/10.1016/j.neuroimage.2012.03.072

Zhu, J., Zhuo, C., Qin, W., Wang, D., Ma, X., Zhou, Y., & Yu, C. (2015). Performances of diffusion kurtosis imaging and diffusion tensor imaging in detecting white matter abnormality in schizophrenia. *NeuroImage: Clinical*, *7*, 170–176. https://doi.org/10.1016/j.nicl.2014.12.008

SUPPORTING INFORMATION

Additional Supporting Information may be found online in the supporting information tab for this article.

How to cite this article: Cabana J-F, Gilbert G, Létourneau-Guillon L, et al. Effects of *SYN1*$_{Q555X}$ mutation on cortical gray matter microstructure. *Hum Brain Mapp*. 2018;39:3428–3448. https://doi.org/10.1002/hbm.24186